

Accepted Manuscript

A thermal multicomponent lattice Boltzmann model

M.K. Ikeda, P. Rao, L.A. Schaefer

PII: S0045-7930(14)00245-X

DOI: <http://dx.doi.org/10.1016/j.compfluid.2014.06.006>

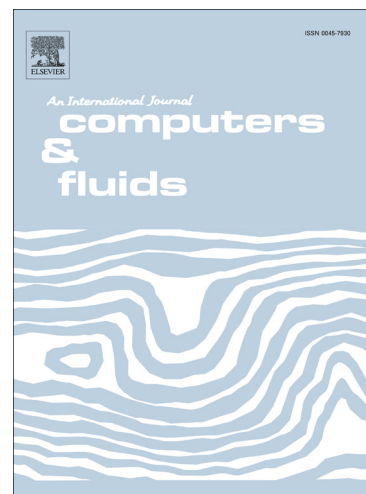
Reference: CAF 2588

To appear in: *Computers & Fluids*

Received Date: 28 March 2013

Revised Date: 12 May 2014

Accepted Date: 5 June 2014



Please cite this article as: Ikeda, M.K., Rao, P., Schaefer, L.A., A thermal multicomponent lattice Boltzmann model, *Computers & Fluids* (2014), doi: <http://dx.doi.org/10.1016/j.compfluid.2014.06.006>

This is a PDF file of an unedited manuscript that has been accepted for publication. As a service to our customers we are providing this early version of the manuscript. The manuscript will undergo copyediting, typesetting, and review of the resulting proof before it is published in its final form. Please note that during the production process errors may be discovered which could affect the content, and all legal disclaimers that apply to the journal pertain.

A Thermal Multicomponent Lattice Boltzmann Model

M. K. Ikeda^{a,*}, P. Rao^a, L. A. Schaefer^a

^a636 Benedum Hall, 3700 O'Hara Street, University of Pittsburgh, Pittsburgh, PA, USA, 15261

Abstract

As energy densities in electronic devices rapidly increase, improved two-phase microchannel heat exchanger designs are of great interest. Similarly, with the implementation of phase separation as a method of flow manipulation in microdevices, understanding the flow dynamics of multiple phases in microchannels is vital. However, experimental studies have thus far shown a great deal of variety in the flow patterns and instabilities that develop at the microscale level. These phenomena are further complicated by the presence of multiple chemical components. Thus, numerical techniques capable of simulating such flow regimes are desirable. The lattice Boltzmann method (LBM) is gaining traction as a powerful approach to fluid flow simulation due to its ability to capture interfacial dynamics without complex interface tracking algorithms. However, existing approaches are currently inadequate for thermal flows with multiple components and multiple phases. In this work, an analysis of the stability region of the interparticle interaction parameters in a multiphase, immiscible, multicomponent, isothermal model is conducted. Informed by this analysis, a multiphase, immiscible, multicomponent, thermal (MPiMC-T) model is constructed using a density-weighted coupling of macroscopic properties. Validation of the model is performed using a static thermal conduction simulation and a steady-state droplet simulation. Conservation properties are maintained and physical consistency is met across component grids in the immiscible limit. Furthermore, a reduction of spurious currents is obtained utilizing the multicomponent framework.

Keywords: lattice Boltzmann method, multiphase flow, multicomponent flow, thermal passive-scalar method, spurious current reduction, interparticle pseudopotential model

1. Introduction

Multicomponent, multiphase flows exist in many engineered systems, such as large-scale nuclear reactors and microscale heat pipes. These

*Corresponding author

Email addresses: mki4@pitt.edu (M. K. Ikeda),
pr28@pitt.edu (P. Rao), las149@pitt.edu (L. A. Schaefer)

flows also are prevalent in nature, like rain and fog. However, little is known about the dynamics of these flows. There is consequently a great deal of interest in developing numerical tools for the simulation of these flow regimes. In the past, most approaches have been based on modifications to traditional computational fluid dynamics (CFD) tools. These involve the addition of interface-tracking or interface-capturing algorithms to the solution of the continuum-based Navier Stokes (NS) equations. Some popular interface-tracking methods are the boundary-fitted grid method [1], Tryggvason's hybrid method [2], and the Boundary Element Method (BEM) [3]. These methods model separate phases and components individually by continually tracking the interfaces and using them as boundary conditions for each flow simulation. However, these techniques require complex, dynamic meshing algorithms and complicated boundary problems. These issues are alleviated through the use of interface-capturing methods, which are the most popular multiphase models currently in use. Examples of interface-capturing methods are the Marker-and-Cell (MAC) method [4, 5], the Volume-of-Fluid (VOF) method [6], and the Level-Set Method (LSM) [7]. These approaches model all phases and components of the flow as a single continuum. Interfaces are then defined as property discontinuities which influence the flow development. These methods have seen moderate success, but

they are still hindered by the complexity of solving both the full NS equations and a coupled algorithm to resolve the interface. This computational complexity has limited these simulations to relatively simple cases. Moreover, all of these methods are artificial approaches to modeling multiphase and multicomponent phenomena. It is well known that phase and component segregation is the consequence of molecular interactions. However, the traditional NS equations neglect any effect of molecular dynamics as they are a purely continuum-based approach. Thus, these methods are all attempts at circumventing a shortcoming of the NS equations.

In this work, the lattice Boltzmann method (LBM) is investigated as an alternative technique for the simulation of multiple phases and components. The LBM is based on a statistical representation of kinetic theory. In this manner, molecular interactions can be incorporated as the driving force behind phase and component separation, avoiding the need to artificially capture or track interfaces. The past two decades have seen a great deal of development in the LBM field, with a number of approaches for implementing molecular interactions. The two models that have shown the most promise are the free energy model proposed by Swift, et al. [8, 9], and the interparticle pseudopotential model, first developed by Shan and Chen [10–12], and later modified separately by Yuan and Schaefer [13, 14] and Kupershtokh

[15, 16]. The free energy model relies on the incorporation of non-equilibrium dynamics, such as the Cahn-Hilliard model, using the concept of the free energy function. This model is physically consistent and, unlike the interparticle pseudopotential model, conserves local momentum. However, Galilean invariance is not satisfied and some unphysical effects have been noted in simulations [17]. The interparticle pseudopotential method instead implements a shift in the local momentum due to the existence of a potential acting between particles in the system. While this leads to a lack of local momentum conservation, global momentum is conserved and phase and component separation occurs spontaneously [10, 12]. It has been shown that the shape of the potential can be controlled by the equation of state in order to produce thermodynamically consistent results [13–16]. As will be shown, the shape of the resulting pseudopotential mimics that of molecular interactions.

In practical engineering problems and natural situations, density ratios between phases and components can vary greatly. For example, the density ratio of a liquid alloy system is around one, while that of water and air can be greater than 1000. The original pseudopotential model proposed by Shan and Chen, which is most commonly implemented in LBM simulations, is limited to density ratios of around two [10, 12]. Therefore, the modified pseudopotential model

developed for high-density ratio multiphase simulations by Yuan and Schaefer [13, 14] and Kupershokh [15, 16], then improved for high-density ratio multiphase, multicomponent systems by Bao and Schaefer [18], is utilized in this work. These developments are based on the incorporation of realistic interparticle potentials via the selection of thermodynamically valid equations of state. In this paper, a thermal passive-scalar model is incorporated into Bao and Schaefer’s multiphase, multicomponent model for the simulation of multiphase, immiscible, multicomponent, thermally-dynamic (MPiMC-T) flows via a density-weighted coupling of hydrodynamic and thermal properties.

2. The lattice Boltzmann Method

The lattice Boltzmann method is based on the numerical solution of the Boltzmann transport equation (BTE). The BTE is a kinetic equation which describes the evolution of the particle distribution function (PDF), $f(\mathbf{x}, \boldsymbol{\xi}, t)$, through time, t , in which $\boldsymbol{\xi}$ and \mathbf{x} are the particle velocity vector and spatial configuration vector, respectively:

$$\frac{\partial f}{\partial t} + \boldsymbol{\xi} \cdot \nabla_{\mathbf{x}} f + \frac{\mathbf{F}}{m} \cdot \nabla_{\boldsymbol{\xi}} f = \Omega. \quad (1)$$

The collision integral, Ω , represents the change in f due to interparticle collisions, \mathbf{F} is a force field, m is the particle mass, and $\nabla_{\mathbf{x}}$ and $\nabla_{\boldsymbol{\xi}}$ are the gradient operators in the configuration and

velocity spaces, respectively. Because of the high dimensions of the distribution function and the complexity of the collision integral, direct solution of the full Boltzmann equation is a formidable task for both analytical and numerical techniques. Therefore, the collision operator is linearized using the Bhatnagar, Gross, and Krook (BGK) approximation [19], which assumes that the effect of the collision between particles is to drive the fluid in a linear fashion towards a local equilibrium state, $f^{(0)}$, i.e. $\Omega = -(f - f^{(0)})/\tau$. This approximation yields the Boltzmann-BGK equation:

$$\frac{\partial f}{\partial t} + \boldsymbol{\xi} \cdot \nabla_{\mathbf{x}} f + \mathbf{a} \cdot \nabla_{\boldsymbol{\xi}} f = -\frac{1}{\tau}(f - f^{(0)}), \quad (2)$$

where τ is the relaxation time, $\mathbf{a} = \mathbf{F}/m$ is the acceleration due to a field, \mathbf{F} , and the equilibrium distribution function (EDF), $f^{(0)}$, is described by the Maxwell-Boltzmann distribution:

$$f^{(0)}(\mathbf{x}, \boldsymbol{\xi}, t) = \frac{\rho(\mathbf{x}, t)}{(2\pi\theta(\mathbf{x}, t))^{\frac{D}{2}}} \exp\left[-\frac{(\boldsymbol{\xi} - \mathbf{u}(\mathbf{x}, t))^2}{2\theta(\mathbf{x}, t)}\right], \quad (3)$$

for the dimension D , and the reduced kinetic temperature, $\theta = k_B T/m$, where k_B is the Boltzmann's constant, T is the absolute physical temperature, and m is the particle mass. The macroscopic density, ρ , and momentum, $\rho\mathbf{u}$ are defined as the first two velocity moments of the PDF:

$$\rho(\mathbf{x}, t) = \int f d\boldsymbol{\xi} \quad (N = 0), \quad (4)$$

$$\rho\mathbf{u}(\mathbf{x}, t) = \int f\boldsymbol{\xi} d\boldsymbol{\xi} \quad (N = 1). \quad (5)$$

The traditional formulations of the LBM by Qian, et al. and Chen, et al. are limited both in their extension to lattice structures and the complexity of the physics that can be recovered [20–22]. Furthermore, they rely upon *a posteriori* coefficient matching in order to enforce Navier-Stokes dynamics. Therefore, this work is instead based on the derivation of the lattice Boltzmann equation as a Hermite series expansion and truncation of the continuum Boltzmann-BGK equation, similar to the Grad 13-moment equation [22, 23]. As a result, the following equations differ slightly from the traditional LBM framework. However, this is purely a scaling effect and it can be shown that when applied to a given lattice structure, the resulting equations combine to match the more traditional forms [22]. Due to the extensibility of this formulation to capturing more complex physical phenomena and its general applicability to complex lattice structures, it is chosen as the basis of this work.

To begin the discretization, the PDFs are first projected onto an orthogonal basis spanned by the Hermite polynomials. A Hermite basis is chosen because a velocity moment of degree N is completely resolved by the expansion coefficients up to that same order N . Thus, lower order moments are not affected by the truncation of higher-order terms [22, 23]. The immensely beneficial consequence of this is that a PDF can be approximated by its projection spanned by the first N Hermite

polynomials, while maintaining exact reproduction of its velocity moments of orders less than or equal to N , just as if the full PDF, without truncation, were utilized in the calculation. Following the derivation by Shan, et al. [22], the projection and truncation of f is expressed mathematically as:

$$\begin{aligned} f(\mathbf{x}, \boldsymbol{\xi}, t) &= \omega(\boldsymbol{\xi}) \sum_{n=0}^{\infty} \frac{1}{n!} \mathbf{a}^{(n)}(\mathbf{x}, t) \mathbf{H}^n(\boldsymbol{\xi}) \\ &\approx f^{(N)}(\mathbf{x}, \boldsymbol{\xi}, t) \\ &= \omega(\boldsymbol{\xi}) \sum_{n=0}^N \frac{1}{n!} \mathbf{a}^{(n)}(\mathbf{x}, t) \mathbf{H}^n(\boldsymbol{\xi}), \end{aligned} \quad (6)$$

where $\mathbf{a}^{(n)}$ and $\mathbf{H}^{(n)}$, both tensors of rank n , are the expansion coefficients and Hermite polynomials, respectively. The weight function associated with the Hermite polynomials, $\omega(\boldsymbol{\xi})$, is defined as:

$$\omega(\boldsymbol{\xi}) = \frac{1}{(2\pi)^{D/2}} \exp\left(-\frac{\boldsymbol{\xi}^2}{2}\right), \quad (7)$$

where $\boldsymbol{\xi}^2 = \boldsymbol{\xi} \cdot \boldsymbol{\xi}$, and the expansion coefficients are given by:

$$\mathbf{a}^{(n)}(\mathbf{x}, t) = \int f(\mathbf{x}, \boldsymbol{\xi}, t) \mathbf{H}^{(n)}(\boldsymbol{\xi}) d\boldsymbol{\xi}. \quad (8)$$

Using the tensor expansion of $\mathbf{H}^{(n)}$, the first few expansion coefficients, which are identified as the hydrodynamic variables of density, momentum, and momentum flux, can be obtained:

$$\rho = a^{(0)}, \quad (9)$$

$$\rho \mathbf{u} = \mathbf{a}^{(1)}, \quad (10)$$

$$\boldsymbol{\Pi} = \mathbf{a}^{(2)} - \rho(\mathbf{u}^2 - \delta). \quad (11)$$

A similar procedure can be applied to the equilibrium distribution function, $f^{(0)}$, to obtain its truncated form and the associated expansion coefficients, $\mathbf{a}_0^{(n)}$. It can be shown through a Chapman-Enskog analysis that, for the recovery of NS level dynamics, the order of truncation of the EDF must be one greater than the order of the velocity moments ($N + 1$). In other words, if momentum is required at the NS level ($N = 1$), the order of truncation of the EDF should be two; if momentum flux and energy are desired, the truncation should be to order three. A detailed description behind this effect is available in the literature [22].

The truncated distribution function, $f^{(N)}$, which is a partial sum of the Hermite series, as shown in Equation (6), can then be uniquely described by its values at a set of discrete nodes, or abscissae. The process of finding a minimum set of abscissae is based on the Gauss-Hermite (GH) quadrature. In short, the Boltzmann-BGK equation can be solved for $f^{(N)}$ by discretizing the velocity space as a set of velocities that correspond to the nodes of the GH quadrature. The rules of the quadrature require the degree of precision of the quadrature, q , to be greater than or equal to $2N + 1$. The most commonly used lattice for 2-D simulations is the D2Q9 structure (nine velocities in two dimensions) shown in Figure 1, which corresponds to a GH quadrature with an algebraic degree of precision of five [22].

Applying a GH quadrature, the Hermite expansion coefficients can be expressed as:

$$\mathbf{a}^{(n)} = \sum_{\alpha=1}^d \frac{w_{\alpha}}{\omega(\boldsymbol{\xi}_{\alpha})} f^N(\mathbf{x}, \boldsymbol{\xi}_{\alpha}, t) \mathbf{H}^{(n)}(\boldsymbol{\xi}_{\alpha}), \quad (12)$$

and defining $f_\alpha(\mathbf{x}, t) = \frac{w_\alpha f^N(\mathbf{x}, \boldsymbol{\xi}_\alpha, t)}{\omega(\boldsymbol{\xi}_\alpha)}$, with $\alpha \in [1, d]$, where d is the number of discrete velocities, yields the following expressions for the macroscopic density and momentum:

$$\rho = \sum_{\alpha=1}^d f_\alpha, \quad (13)$$

$$\rho \mathbf{u} = \sum_{\alpha=1}^d f_\alpha \boldsymbol{\xi}_\alpha. \quad (14)$$

The D2Q9 model used in this work has the following form of lattice velocities and weights [20, 22]:

$$\boldsymbol{\xi}_\alpha = \begin{cases} (0, 0), & \alpha = 1; \\ (\pm\sqrt{3}, 0), (0, \pm\sqrt{3}), & \alpha = 2, 3, 4, 5; \\ (\pm\sqrt{3}, \pm\sqrt{3}), & \alpha = 6, 7, 8, 9. \end{cases} \quad (15)$$

$$w_\alpha = \begin{cases} 4/9, & \alpha = 1; \\ 1/9, & \alpha = 2, 3, 4, 5; \\ 1/36, & \alpha = 6, 7, 8, 9. \end{cases} \quad (16)$$

The discrete formulation of the Boltzmann-BGK then takes the form:

$$\frac{\partial f_\alpha}{\partial t} + \boldsymbol{\xi}_\alpha \cdot \nabla_{\mathbf{x}} f_\alpha = -\frac{1}{\tau} [f_\alpha - f_\alpha^{(0)}] + \mathbf{F}_\alpha, \quad (17)$$

where the discrete form of the equilibrium distribution function, up to the second order as required for the simulation of NS level dynamics, is given as [24]:

$$f_\alpha^{(0)} = w_\alpha \rho \left\{ 1 + \underbrace{\boldsymbol{\xi}_\alpha \cdot \mathbf{u}}_{\text{1st order}} + \underbrace{\frac{1}{2} [(\boldsymbol{\xi}_\alpha \cdot \mathbf{u})^2 - u^2 + (\theta^* - 1)(\xi_\alpha^2 - D)]}_{\text{2nd order}} + \dots \right\}, \quad (18)$$

where $u^2 = \mathbf{u} \cdot \mathbf{u}$ and $\xi_\alpha^2 = \boldsymbol{\xi}_\alpha \cdot \boldsymbol{\xi}_\alpha$. The relative kinetic temperature, $\theta^* = \theta/\theta_0$, represents the variation of the kinetic temperature with respect to the characteristic kinetic temperature θ_0 , under the assumption that this variation is small (i.e. θ^* remains close to one) [24]. For an isothermal system, θ^* is exactly one and the corresponding terms drop out of the expression [22].

Finally, to solve these equations numerically, Equation (17) is discretized in space and time. The most common procedure is to first utilize forward differencing in time, followed by upwinding and downwinding for the convection and collision terms, respectively. This leads to the well-established, second-order form of the fully discretized LB equation [25, 26]:

$$f_\alpha(\mathbf{x} + \Delta \mathbf{x}, t + \Delta t) - f_\alpha(\mathbf{x}, t) = -\frac{1}{\tau} [f_\alpha(\mathbf{x}, t) - f_\alpha^{(0)}(\rho, \mathbf{u})] + \mathbf{F}_\alpha, \quad (19)$$

where $\Delta \mathbf{x} = \boldsymbol{\xi}_\alpha \Delta t$ for a timestep of Δt . The force term is implemented in this work using the exact difference method (EDM) developed by Kupershstokh [27]. This method treats the force as a perturbation to the PDFs and leads to the following modified form of the discrete LBE:

$$f_\alpha(\mathbf{x} + \Delta \mathbf{x}, t + \Delta t) - f_\alpha(\mathbf{x}, t) = -\frac{1}{\tau} [f_\alpha(\mathbf{x}, t) - f_\alpha^{(0)}(\rho, \mathbf{u})] + \Delta f_\alpha, \quad (20)$$

where,

$$\Delta f_\alpha = f_\alpha^{(0)}(\rho, \mathbf{u} + \Delta \mathbf{u}) - f_\alpha^{(0)}(\rho, \mathbf{u}), \quad (21)$$

and $\Delta \mathbf{u} = \mathbf{F} \Delta t / \rho$.

Any number of forces, such as body forces and the forces that result from interparticle interactions, can be incorporated in the same way [13, 28]. Forces are simply summed to determine the total force acting on a given particle within the system:

$$\mathbf{F}_{total} = \mathbf{F}_{body} + \mathbf{F}_{interparticle} + \cdots, \quad (22)$$

which is then incorporated into the LB model through the EDM. The macroscopic, physical velocity is then taken as the average between the pre- and post-shifted velocities as [29]:

$$\mathbf{u}^* = \mathbf{u} + \frac{\mathbf{F}\Delta t}{2\rho}. \quad (23)$$

From a Chapman-Enskog expansion under the low Mach number assumption, it can be shown that the lattice Boltzmann equation with these discretizations corresponds to the Navier-Stokes equations with a kinematic viscosity of [17, 24, 30]:

$$\nu = \left(\tau - \frac{1}{2}\right) c_s^2 \Delta t, \quad (24)$$

where c_s is the lattice speed of sound and is equal to $c/\sqrt{3}$, where $c = |\boldsymbol{\xi}_\alpha|$, is the lattice spacing per time step. It should be noted that this formulation is consistent with the variations of the EDF that are derived from coefficient matching approaches, rather than Hermite polynomial expansions. This can be verified by scaling the lattice velocity vectors, $\boldsymbol{\xi}_\alpha$, by their magnitude to recover the traditional formulation of the velocities [22]. For consistency, the macroscopic velocities

in the EDF expression must also be scaled, which leads to the traditional formulation of the EDF as well. This formulation is chosen for its mathematical rigor and its extensibility to higher-order lattices and more complex physical phenomena [22].

3. Multiphase Pseudopotential Method

Phase separation, as well as the separation of chemical components, occurs due to long-range molecular interactions. To incorporate these interactions into the LBM, many methods have been developed. The Shan and Chen (SC) model of interparticle pseudopotentials is the original method and is still the most versatile [10–12, 26, 31]. In the SC model, the interparticle potential in the long wavelength limit is defined as [10, 14, 22]:

$$V = c_0 g_f \psi^2, \quad (25)$$

where $c_0 = bc^2/2D$, b is the number of neighbors, equal to 8 for the D2Q9 model, g_f is a parameter which controls the strength of the interaction, and ψ is an effective mass. It can be shown that the effective mass can be related to the pressure of the system, p , as [11, 17]:

$$p = c_s^2 \rho + c_0 g_f \psi^2, \quad (26)$$

where the term with the effective mass represents the deviation from ideality. In the original SC model, the effective mass is written for a simple, non-ideal equation of state as:

$$\psi = \rho_0 \left[1 - \exp\left(\frac{-\rho}{\rho_0}\right) \right], \quad (27)$$

for a reference density, ρ_0 . However, this formulation corresponds to an equation of state in which the liquid phase is highly compressible [31]. To mitigate this problem, Yuan and Schaefer [13, 14] and Kupershtokh, et al. [15, 16] separately implemented thermodynamically consistent models by calculating the effective mass using a pressure found directly from realistic equations of state. This is based on the formulation of the effective mass in terms of the pressure expressed by He and Doolen [24] and Nourgaliev, et al. [17]:

$$\psi = \sqrt{\frac{p - c_s^2 \rho}{c_0 g_f}}. \quad (28)$$

For the Peng-Robinson EOS used in this work, the pressure is calculated as:

$$p = \frac{\rho RT}{1 - b\rho} - \frac{a\alpha_{PR}\rho^2}{1 + 2b\rho - b^2\rho^2}, \quad (29)$$

where $a = 2/49$, $b = 2/21$, and α_{PR} is:

$$\alpha_{PR} = \left[1 + \eta \left(1 - \sqrt{\frac{T}{T_c}} \right) \right]^2. \quad (30)$$

In these expressions, η is defined as:

$$\eta = (0.37464 + 1.54226\omega - 0.26992\omega^2), \quad (31)$$

ω is the acentric factor of the substance and T_c is the critical temperature. The resulting pseudopotential, V , is shown in Figure 2. It can be seen that this formulation leads to an attractive core and repulsive tail, mimicking the effect of molecular interactions. This pseudopotential is incorporated into the LBM by calculating the force that

results due to its presence:

$$\begin{aligned} \mathbf{F}_{interparticle} &= -\nabla_x V, \\ &= -\nabla c_0 g_f \psi^2. \end{aligned} \quad (32)$$

The gradient operator is discretized in space using a method developed by Kupershtokh which involves taking a linear combination of the local and the mean value gradient approximations (LCGA), leading to the following formulation of the interparticle force [15, 16]:

$$\begin{aligned} \mathbf{F}_{interparticle} &= -2c_0 g_f \left[\underbrace{A_{kup} \nabla_x \psi^2}_{\text{Mean Value}} \right. \\ &\quad \left. + \underbrace{(1 - 2A_{kup}) \psi \nabla_x \psi}_{\text{Local}} \right], \end{aligned} \quad (33)$$

for a correlative fitting parameter defined by Kupershtokh, A_{kup} , and the lattice dependent parameters, c_0 , defined previously. This equation has a slightly different formulation than that originally presented by Kupershtokh due to the implementation of the effective mass instead of Kupershtokh's special function, Φ . The effective mass is used here in reference to the work by Yuan and Schaefer [13, 14]. These parameters can be related as $\psi = \Phi / \sqrt{-c_0 g_f}$, which leads directly to the expression developed by Kupershtokh [15, 16, 32]. The spatial gradients are discretized in this work using a standard weighted average of 2D central differences [33, 34].

The combination of the generalized expression of the effective mass and Kupershtokh's correlative calculation of the discrete gradient operator

greatly increases the stability of the LBM to simulate high density ratio, multiphase flows, previously a severe limitation of the SC model. For the Peng-Robinson equation of state, a value of $A_{kup} = -0.1125$ has been shown to yield an accurate reproduction of the binodal curves, as shown in Figure 3, in comparison to pure local or pure mean value approximations. Furthermore, due to the increased fidelity of the density ratio calculation, a large decrease in the spurious currents that typically plague many multiphase simulations is achieved. This enables the stable simulation of lower temperatures and higher-density ratios using the LBM. In this work, we have simulated density ratios up to 850:1 using simple numerics. It has been shown that even higher density ratios, on the order of 1 million, are also possible utilizing this framework with more complex and dissipative numerics [15, 32].

4. Thermal Model

There are a variety of methods in which thermal effects can be incorporated into the LBM. The most popular and straightforward approach is the passive-scalar method [35]. In this approach, the physical temperature, not the kinetic temperature, is passively advected by the hydrodynamics of the system. Neglecting the viscous and compressive heating effects, as well as any heat sources, the physical temperature, T , obeys

the PDE:

$$\frac{\partial T}{\partial t} + \mathbf{u}^* \cdot \nabla T = \nabla \cdot (\hat{\alpha} \nabla T), \quad (34)$$

where \mathbf{u}^* is the macroscopic, physical velocity defined in Equation (23) and $\hat{\alpha}$ is the thermal diffusivity. Due to the passive nature of the temperature field, this equation can be solved by the same method as the density by simply defining a second PDF corresponding to the temperature, $g_\alpha(\mathbf{x}, t)$, such that:

$$g_\alpha(\mathbf{x} + \Delta \mathbf{x}, t + \Delta t) - g_\alpha(\mathbf{x}, t) = -\frac{1}{\tau_T} [g_\alpha(\mathbf{x}, t) - g_\alpha^{(0)}(T, \mathbf{u}^*)], \quad (35)$$

where τ_T is a dimensionless relaxation time corresponding to the rate at which the temperature dynamics approach their equilibrium. The thermal equilibrium PDF takes the same form as Equation (18) for a second order method:

$$g_\alpha^{(0)} = w_\alpha T \left[1 + \boldsymbol{\xi}_\alpha \cdot \mathbf{u}^* + \frac{1}{2} (\boldsymbol{\xi}_\alpha \cdot \mathbf{u}^*)^2 - \frac{1}{2} u^{*2} \right]. \quad (36)$$

The temperature, as with the density, is then just the sum of the thermal PDFs:

$$T = \sum_{\alpha=1}^d g_\alpha, \quad (37)$$

and the thermal diffusivity can be defined for this formulation just as the viscosity was previously, giving:

$$\hat{\alpha} = (\tau_T - \frac{1}{2}) c_s^2 \delta t, \quad (38)$$

which leads to a variable Prandtl number of:

$$Pr = \frac{\nu}{\hat{\alpha}} = \frac{2\tau - 1}{2\tau_T - 1}. \quad (39)$$

It is important to note three assumptions and limitations of this model. First, although the thermal passive-scalar method is solved using as a secondary PDF, this does not imply a kinetic interpretation of the temperature. Instead, a secondary PDF is used only as a numerical discretization method of the physical temperature evolution equation. The kinetic temperature is assumed constant ($\theta^* = 1$) through a single time step, with the physical temperature being advected only by the hydrodynamics of the system. Second, Equation (34) does not include any influence of the latent heat and consequently, the simulations based on this model are restricted to those which do not include phase change. Future work will include models that have incorporated such effects [36–40]. Finally, as with the viscosity, the thermal diffusivity is determined by a single, constant relaxation time and therefore does not vary spatially or temporally, regardless of the phase.

5. Boundary Conditions

In this work, the Zou-He boundary condition (ZHBC) is used for solid walls [41]. The ZHBC only replaces the unknown PDFs, leaving the rest unmodified. This construction corresponds to a fictitious fluid element outside of the domain that streams into the boundary node in order to elicit the correct hydrodynamic conditions at that boundary node. A full description of the formu-

lation and implementation is given by Zou and He [41], as well as by Latt and Chopard [42]. The ZHBC was chosen for its local nature (only PDFs at the local node are required) and its explicit form in both two and three dimensions. The ZHBC has been shown to be stable at moderately low Reynolds numbers and is second order accurate on straight wall boundaries while reproducing the no-slip condition at the boundary.

For open boundaries, the periodic condition is used. This BC is applied directly to the post-collision PDFs as:

$$f_{\alpha}(\text{inlet}) = f_{\alpha}(\text{outlet}) \quad \forall \quad \alpha \in [1, d]. \quad (40)$$

For an isothermal wall at temperature T_w , the unknown thermal PDFs are assumed to take the form of their equilibrium distribution, as given in Equation (36), with an unknown temperature T' . This unknown temperature can then be determined using the prescribed wall temperature. For example, for the D2Q9 model shown in Figure 1, at a fixed lower boundary, the expression becomes:

$$T' = 6(T_w - g_0 - g_1 - g_3 - g_4 - g_7 - g_8), \quad (41)$$

where the sum of the unknown PDFs has been replaced by the sum of their equilibrium distributions. Using the equilibrium distribution equation again with the value of T' gives the unknown PDFs.

6. Multicomponent Model

The existence of more than one chemical component adds a great deal of complication to a system's dynamics. However, the lattice Boltzmann method benefits from the ability to treat each component using a separate PDF. For instance, in a system of two components, Component A and Component B , one set of PDFs will represent Component A ($f_{\alpha,A}$) and another set will represent Component B ($f_{\alpha,B}$). Each set of PDFs can be evolved separately following the lattice Boltzmann equation, and the velocity moments of one PDF will represent the density and momentum of only that component:

$$\rho_{A,LU} = \sum_{\alpha=1}^d f_{\alpha,A}, \quad (42)$$

$$\rho_{B,LU} = \sum_{\alpha=1}^d f_{\alpha,B}, \quad (43)$$

$$\rho_{A,LU} \mathbf{u}_{A,LU} = \sum_{\alpha=1}^d f_{\alpha,A} \boldsymbol{\xi}_{\alpha}, \quad (44)$$

$$\rho_{B,LU} \mathbf{u}_{B,LU} = \sum_{\alpha=1}^d f_{\alpha,B} \boldsymbol{\xi}_{\alpha}. \quad (45)$$

The subscript LU is used to denote that the densities and velocity vectors are represented in the lattice domain.

The components are allowed to interact with each other in a manner similar to the phase interactions. In this case, the interparticle pseudopotentials correspond to the attraction and repulsion of the different chemical components, instead of the phases [26]. The multiphase and multicomponent models have recently been combined

by Bao and Schaefer, along with the implementation of advanced equations of state, to formulate a high-density ratio, multiphase, multicomponent model [18, 28, 43]. The intercomponent force acting on a particle of Component A due to a particle of Component B , takes the form:

$$F_{A,B} = c_0 \psi_A g_{A,B} \nabla \psi_B, \quad (46)$$

where $c_0 = 6$ for the D2Q9 model, and $g_{A,B}$ is an interparticle interaction strength parameter that controls the interaction between the A and B chemical components. The domain for a two component simulation is configured by overlaying two numerical grids, one for each component. Each grid contains information about the PDFs, the density, the temperature, and the effective mass of its own component. As before, the particles within one grid are allowed to interact with themselves (intracomponent interaction) through the multiphase interactions already discussed. However, these particles can now also interact with the particles from the other grid (intercomponent interactions) through Equation (46). The grid corresponding to Component A will be influenced by $F_{A,B}$ via the exact difference method. Similarly, the grid which contains information about Component B will be influenced by the intercomponent force $F_{B,A}$, the strength of which is controlled by parameter $g_{B,A}$.

An example initialization of the two grids for a 2D simulation based on the two phase, two component model is illustrated in Figure 4. Grid one

has a high-density, liquid region of Component A at its center and is surrounded by a zero-density region. On grid two, the nodes corresponding to the liquid region on grid one are initialized as a zero-density region and the nodes corresponding to the zero-density region on grid one are the low-density, vapor region of Component B . It is important to note that a true, zero-density region is not feasible in a numerical simulation. Implementation of such a region would lead to discontinuities in the gradient calculations and divergence of the simulation. Figure 4 shows the zero-density regions to have densities of exactly zero; however, this is just for clarity of explanation. In practice, it is necessary that in regions which are indicated as having zero-densities, small non-zero values are used. Thus, when the zero-density region is referred to throughout this work, the region is actually implemented as a low density region. As will be discussed later, it is necessary to verify that this small value is actually small enough that the effect of this region is minimized in order to maintain an accurate simulation of immiscible substances.

Isothermal simulations are performed of a liquid water droplet surrounded by air in a fully periodic domain. The reduced density cross-sections at $T = 450$ K and $T = 600$ K are shown in Figures 5a and 5b. The cross-sections are taken at the horizontal centerline ($y = 50$ LUs). The density ratio at $T = 450$ K is 152:1 and at $T = 600$

K is 13:1. The zero-density regions can also be seen in both of these figures as the lower density section of each line. Importantly, these zero-density regions have densities greater than zero, but less than the primary phase in that region. Specifically, the zero-density regions of the water ($\text{Water}_{\text{zero}}$) lie below the vapor regions of the air ($\text{Air}_{\text{vapor}}$) and the zero-density regions of the air (Air_{zero}) lie below the liquid regions of the water ($\text{Water}_{\text{liquid}}$). This ensures that the behavior exhibited by the interphase and intercomponent interactions is dominated by the phases of interest, rather than the zero-density regions. As the low density used to approximate the zero-density regions is further decreased, the fidelity of the simulation will improve, but this is at the cost of steeper gradient calculations, which eventually will diverge.

7. Multicomponent Thermal Model

While Bao and Schaefer have greatly improved the multiphase, multicomponent LBM [18, 28], thermal effects have not yet been incorporated into these models. This is an important aspect, as many of the engineering systems of interest have significant temperature variations. However, adding a passive-scalar model to the multicomponent framework leads to complications with the intercomponent interparticle interaction parameters and contradictions with regards to the macroscopic variables. These two issues are addressed

in the following sections.

7.1. Stability Analysis of Interaction Parameters

One particular concern is the stability of the simulation at different values of intercomponent interaction strength parameters ($g_{A,B}$ and $g_{B,A}$). Thus far, nothing was said concerning the magnitude or determination of these parameters. Before delving into the thermal model, it is necessary to better understand the effects that the variation of these parameters have on the model's stability. To that end, a stability region analysis is undertaken to examine the interparticle interaction parameter ranges which lead to stable simulations. In this study, the $g_{A,B}$ and $g_{B,A}$ parameters are varied independently over a wide range. This range was chosen such that the stability domain is bounded over the set of temperatures considered. It must be emphasized that this is purely a stability analysis and does not consider the physical implication that the parameters should be equal. This consideration is made due to the instability that arises when the parameters are in fact equated. It is likely that this instability exists due to the numerics of the system. Future investigations of dissipative schemes would be beneficial in order to shed some light on this. It is found that there are three possible outcomes: 1) convergence to a stable and valid density ratio, 2) complete divergence of the simulation, or 3) convergence to a stable, but erroneous density ratio. An erroneous density ratio here is defined as one in which the density

of the vapor phase component is less than that of the zero-density region of the liquid phase component. An example of such a system is shown by the reduced density cross-sections depicted in Figure 6. As discussed previously, it is not possible to use a true zero-density region and consequently, the zero-density regions actually correspond to small, non-zero values. However, for certain values of $g_{A,B}$ and $g_{B,A}$, this causes problems. When the vapor phase of Component B ($\text{Air}_{\text{vapor}}$ in the case of Figure 6) has a density smaller than that of the zero-density region of Component A ($\text{Water}_{\text{zero}}$ in Figure 6), the interaction between the liquid phase of Component A and the zero-density region of Component A ($\text{Water}_{\text{liquid}}$ and $\text{Water}_{\text{zero}}$) is greater than the interaction between the liquid phase of Component A and the vapor phase of Component B ($\text{Water}_{\text{liquid}}$ and $\text{Air}_{\text{vapor}}$). While this may be valid for a miscible, multicomponent mixture, if immiscible dynamics are intended, such a simulation will yield inaccurate behavior. In this work, immiscibility is desired, for reasons which will be discussed later, and therefore the parameters which lead to this state are indicated separately in this analysis and are not considered to be part of the valid stability region.

The stability analysis is performed for a variety of temperatures to determine the stability region for each temperature. Examples of these results are shown in Figures 7a and 7b, for $T = 450$ K and $T = 625$ K. Clearly, the region of stability shifts

as the temperature changes. This highlights the importance of this study. If only a single temperature is used to find stable parameters, it is possible that in a thermal simulation, temperature changes could lead to unstable simulations. Therefore, from this information, the overlap in the stability regions is analyzed by selecting only interaction pairs that are stable across all of the temperatures considered. In this manner, a set of parameters can be found that will, in a thermal study, continue to yield stable and valid density ratios as the temperature of the simulation varies. Figure 8 displays the region of overlap between simulations performed at $T=[450 \text{ K}, 500 \text{ K}, 550 \text{ K}, 600 \text{ K}, 625 \text{ K}]$, and it can be seen that values of $g_{A,B}=0.05$ and $g_{B,A}=0.005$ will maintain stability over thermal variations spanning this temperature range, at a minimum.

7.2. Reconstruction of Macroscopic Variables

With the interaction parameters well-defined, a treatment of the thermal phenomena in the multiphase, multicomponent model can now be evaluated. For a binary fluid with thermal effects and multiple phases, four equations must be considered: a hydrodynamic evolution equation and a thermal evolution equation for each component. However, as shown in Equations (44) and (45), there are separate velocities for each component despite the fact that these occur on overlapping nodes of the two numerical grids (i.e. at the same spatial location). Similarly, the same will oc-

cur for the temperatures, with the corresponding nodes on the two grids having potentially different temperature values. Clearly, this is not physically consistent as the same point in space must have only a single velocity vector and a single temperature. Therefore, the primary difficulty lies in the reconstruction of the macroscopic velocity and temperature information from multiple equations.

First, independent thermal PDFs are solved, one for each chemical component. The coupling of the temperatures is carried out post-streaming using a density-weighted combination of the physical temperatures, such that $T_{coupled,p}$ is defined as:

$$T_{coupled,p} = \frac{\sum_{i=1}^N \rho_{i,p} T_{i,p}}{\sum_{i=1}^N \rho_{i,p}}, \quad (47)$$

where the subscript p denotes the values are in physical units, i runs from 1 to N components, and the temperatures are found from independently treated PDFs, just as the densities were in the isothermal model described above. In the two component case where $i = 1$ corresponds to Component A , and $i = 2$ corresponds to Component B , Equation (47) becomes:

$$T_{coupled,p} = \frac{\rho_{A,p} T_{A,p} + \rho_{B,p} T_{B,p}}{\rho_{A,p} + \rho_{B,p}}. \quad (48)$$

These formulations are only valid for substances with equal specific heats and for a passive-scalar model in which the temperature itself, not the energy, is advected without phase change. If different thermodynamic properties or phase transitions are to be modeled, these equations would need to be modified accordingly. Additionally,

it is necessary, when carrying out the temperature coupling, to utilize temperatures and densities in the physical domain. The physical values are found by first calculating the macroscopic variables in the lattice domain using Equations (42), (43), and:

$$T_{A,LU} = \sum_{\alpha=1}^d g_{\alpha,A}, \quad (49)$$

$$T_{B,LU} = \sum_{\alpha=1}^d g_{\alpha,B}, \quad (50)$$

where the subscript LU corresponds to values in lattice units. Along with the densities these values can be translated to the physical domain using the reduced properties [14]:

$$\rho_{A,p} = \rho_{A,LU} \frac{\rho_{c,p}}{\rho_{c,LU}}, \quad (51)$$

$$\rho_{B,p} = \rho_{B,LU} \frac{\rho_{c,p}}{\rho_{c,LU}}, \quad (52)$$

$$T_{A,p} = T_{A,LU} \frac{T_{c,p}}{T_{c,LU}}, \quad (53)$$

$$T_{B,p} = T_{B,LU} \frac{T_{c,p}}{T_{c,LU}}. \quad (54)$$

It is important in the case of temperatures to use values in the physical domain for the coupling carried out in Equations (47) and (48), as it is the physical temperatures, not the lattice temperatures, which must be equal for thermodynamic consistency. The reason for this is clear when it is recalled that the critical temperatures in the lattice domain are constant across different chemical components. Thus, two different components, both with the same physical temperature but different physical critical temperatures, will actually

have two different lattice temperatures. The temperature can be converted back into lattice units post-coupling to form two different coupled temperatures, one for each component, but representing the same physical value:

$$T_{A,coupled,LU} = T_{coupled,p} \frac{T_{c,LU}}{T_{c,p}}, \quad (55)$$

$$T_{B,coupled,LU} = T_{coupled,p} \frac{T_{c,LU}}{T_{c,p}}. \quad (56)$$

These values are then used to evaluate the effective masses of each of the components, which can be used for the determination of interparticle and intercomponent potentials.

The velocity information obtained from the two hydrodynamic equations must also be combined. The method used to select the velocities must be done in such a way that consistency is maintained and momentum is conserved globally. The coupled velocity is therefore also calculated via weighting by the densities at each node:

$$\mathbf{u}_{coupled,LU} = \frac{\sum_{i=1}^N \rho_{i,LU} \mathbf{u}_{i,LU}}{\sum_{i=1}^N \rho_{i,LU}}. \quad (57)$$

As noted by the subscripts, this coupling can be carried out in the lattice domain. The single velocity vector and the two coupled temperatures (all in lattice units), are then utilized in the calculation of the thermal equilibrium PDFs:

$$g_{\alpha,A}^{(0)} = w_{\alpha} T_{A,coupled,LU} \left[1 + \boldsymbol{\xi}_{\alpha} \cdot \mathbf{u}_{coupled,LU} + \frac{1}{2} (\boldsymbol{\xi}_{\alpha} \cdot \mathbf{u}_{coupled,LU})^2 - \frac{1}{2} u_{coupled,LU}^2 \right], \quad (58)$$

$$g_{\alpha,B}^{(0)} = w_{\alpha} T_{B,coupled,LU} \left[1 + \boldsymbol{\xi}_{\alpha} \cdot \mathbf{u}_{coupled,LU} + \frac{1}{2} (\boldsymbol{\xi}_{\alpha} \cdot \mathbf{u}_{coupled,LU})^2 - \frac{1}{2} u_{coupled,LU}^2 \right]. \quad (59)$$

These equilibrium PDFs are subsequently used in the collision steps of the separate thermal evolution equations for the corresponding components. This approach is consistent due to the fact that both components occupying the same spatial area will equilibrate toward the same thermal equilibrium in the physical domain.

By enforcing the immiscibility of the components through proper interparticle interaction parameters, as discussed previously, this approach should maintain the same conservation properties as the single-component model. An error will exist due to the inability to simulate true zero-density regions in the numerical scheme, but this can be minimized by maintaining a sufficiently large ratio between the phases of interest and the zero-density regions (i.e. ensuring the interaction parameters do not approach regions of density errors, as discussed during the stability analysis). The thermal model is analyzed by considering the cases of a static thermal conduction simulation and a static liquid droplet simulation with steady-state spurious currents.

8. Multiphase, Immiscible, Multicomponent, Thermal (MPiMC-T) Simulation Results

8.1. Static Thermal Conduction Simulation

The numerical scheme is first tested to ensure that it is capable of reproducing realistic thermal behavior in a simple, static system. In order to

evaluate this concept, a thermal conduction simulation is performed. Figure 9 shows the residual temperature error between the simulation results and the theoretical value with increasing the grid resolution. This is calculated as:

$$T_{\text{Residual}} = \frac{\sum_{j=1}^J |T_{LBM,j} - T_{theor,j}|}{J}, \quad (60)$$

where the index represents the nodes along the vertical cross-section. Grid independence is achieved to a reasonable degree at a domain height, J , of 200 LU. Thus, a 2D channel, 200 LUs tall and periodic in the x -direction is considered. The two component thermal model is utilized, but both components are initialized as liquid water at 550 K to avoid any complications from differing chemical properties. As shown in Figure 10, the domain is initialized with two horizontal liquid layers of water. The top and bottom walls are fixed at 545 K and 555 K, respectively, and the inside of the domain is initialized as 550 K.

The simulation is evolved through time, as depicted by the reduced temperature vertical cross-sections of grid one in Figure 11, until reaching a steady state. The colorbar in the figure represents the timesteps, with darker lines corresponding to later times. The final reduced density vertical cross-sections of the simulation are shown in Figure 12a. The separate liquid components are shown with the existence of the diffuse interface at the intersection of the two components. Reduced temperature contours are also depicted in

12b. The final state is seen to be the correct linear conduction profile that is expected in a static system, verifying that the thermal model is functioning correctly, despite the presence of two distinct phases. Figure 13 shows the residual temperature error, calculated as before, as the simulation progresses through time. It can be seen that the simulation is rapidly equilibrating to the theoretical linear conduction profile. Comparing Figures 11 and 12a, the linearity of the profile is maintained through the diffuse interface where the two components intersect as well.

The importance of the coupling models can now be examined by comparing the error between the temperatures and velocities of the two grids. For any given node, the physical temperature and the velocities must be equivalent. When both the velocities and temperatures are coupled, the errors between the grids will be zero as the values of both grids are set to the coupled values. However, it is possible to relax the coupling constraint on the temperatures, the velocities, or both, and examine the error that arises by comparing, at each time step, the values of the two different grids. The temperature error is calculated in the physical domain as:

$$T_{error,p} = \sum_{\text{all nodes}} \frac{|T_{A,p} - T_{B,p}|}{\# \text{ of nodes}}, \quad (61)$$

and the errors in the magnitudes of the velocities

are calculated for the 2D case in lattice units as:

$$|V|_{error} = \sum_{\text{all nodes}} \frac{\sqrt{(u_{x,A} - u_{x,B})^2 + (u_{y,A} - u_{y,B})^2}}{\# \text{ of nodes}}. \quad (62)$$

These errors are plotted in Figure 14 for the thermal model for the four cases of no coupling of any kind, only temperature coupling, only velocity coupling, and both velocity and temperature coupling. By definition, the temperature-coupled model will have no temperature error, the velocity-coupled model will have no velocity error, and the combined model will have no error at all. It can be seen that the final solution for this particular example converges for all models. Therefore, no coupling is necessary for a steady state, static model. However, the dynamics of the simulation are affected by the numerical scheme. In this simulation, the total temperature error between the two grids was greater than 10% of the total initial temperature difference during the early stages of the simulation. The coupling process removes the discrepancy between the two grids throughout the simulation for the temperatures and the the velocities. These results verify the thermal model in the static case; however, the steady-state flow case needs to be analyzed as well. For this, the static droplet simulation is utilized.

8.2. Static Droplet Simulation

A liquid water droplet surrounded by water vapor is simulated in a fully periodic domain at

500 K with $g_{A,B} = 0.05$ and $g_{B,A} = 0.005$. The simulation is performed using the thermal two-component model so that the phases maintain immiscibility. At steady-state, the reduced liquid and vapor densities are found to be approximately 2.9 and 0.05, respectively, giving a density ratio of 52. This is as compared to data from the NIST WebBook of approximately 2.6 and 0.04 for the reduced liquid and vapor densities, respectively, corresponding to a density ratio of 63, showing reasonable agreement [44]. Mass and momentum conservation are considered first for the model with no coupling, temperature-coupling only, velocity-coupling only, and both temperature and velocity coupling. These are verified in all cases. This is to be expected given the formulation of the coupling models (the velocity coupling is constructed such that conservation is ensured) and the implementation of a full periodic domain (no mass or momentum can enter or leave the system).

Next, the internal energy conservation of the models is analyzed, the results of which are given in Figure 15. It is found that the temperature-coupling model used alone leads to a large violation of internal energy conservation, whereas the other models behave correctly. In fact, the error in energy conservation is so severe that it leads to the rapid divergence of the simulation. This is a result of the erroneous temperature profile causing density ratios too large to be handled by the

LBM. It should be noted that the model with no coupling will always conserve mass, momentum, and energy for a full periodic domain; however, the model is physically incorrect as it allows a discrepancy between the macroscopic properties of nodes between the different numerical grids. This is clear when the model errors are considered again, as in the previous section. The temperature error and velocity magnitude error are shown for the static droplet simulation in Figure 16. These results confirm that the model used without any coupling, as well as the temperature-coupled model used alone, yield physically inconsistent results. Furthermore, the influence of steady-state flow can be seen to lead to a persistent error, unlike the static case in which all of the models eventually converged.

A closer inspection of the velocities leads to insight into the performance of the models. Figures 17a and 17b show a comparison of the velocity vectors of the steady-state solution of the static droplet simulation for the model with no coupling and the model with both temperature and velocity coupling, respectively. The left hand sides of the figures show the first grid (a liquid water droplet surrounded by a zero-density region) and the right-hand sides show the second grid (water vapor surrounding a zero-density bubble). The shaded region in the center of the domain shows the location of the liquid droplet. As can be seen, the maximum velocity magnitudes in the coupled

model are lower than the magnitudes of the model without coupling. The maximum magnitude is reduced from 0.01483 to 0.01029 for water at a temperature of 500 K. Additionally, the currents inside the droplet area nearly disappear. (It should be noted that these spurious currents are specifically for the Peng-Robinson EOS used in this simulation. Many other equations of state have been tested in a variety of other simulations that show differing levels of stability.) This is due to the fact that the spurious currents that are a consequence of the anisotropies in the discrete gradient operator occur primarily in the zero-density regions (outside the liquid droplet on the first grid and inside the zero-density bubble on the second grid). Weighting via the densities therefore aids in the reduction of the effect of these spurious currents. Nevertheless, the spurious currents persist in the model. The errors in conservation and the discrepancies between the two grids exist in this case only as a result of the spurious currents. This is why the static case of thermal conduction led to eventual convergence for all models, whereas the steady-state flow case does not. Therefore, by reducing the influence of the spurious currents, the accuracy of the models can be improved. This reduction is limited by the inability to simulate a true zero-density region. However, this represents a limitation in the numerics of the simulation, not the LBM approach itself. Further work is being done at this time to implement numerical schemes

capable of supporting larger gradients stably and accurately. In this manner, it is thought that the effect of the spurious currents can be further reduced in the future.

9. Conclusion

In conclusion, a multiphase, immiscible, multi-component thermal lattice Boltzmann model has been developed and tested. The model is based on Yuan and Schaefer's and Kupershtokh's modifications to Shan and Chen's interparticle pseudopotential model and Kupershtokh's correlative gradient calculation. These approaches allow the simulation of high-density ratio flows. Thermal effects are incorporated using the passive-scalar model and a density-weighted coupling of physical properties. The model has been tested using static thermal conduction and steady-state droplet simulations. The fully-coupled model is shown to conserve mass, momentum, and energy and maintains the physical requirement that the macroscopic properties are consistent at overlapping spatial locations. It must be emphasized, however, that this model is only evaluated under steady-state conditions here with the assumption of constant thermodynamic properties across phases and without the presence of phase change. Future work will focus on the validation of the model under dynamic flow conditions. It is thought that the errors resulting from the existence of a diffuse interface between the compo-

nents may have a more profound effect in the dynamic problem. Thus, techniques for improving the stability of the interface will likely need to be investigated as part of the dynamic study.

It has also been shown that the multicomponent framework can be utilized as a method for the reduction of spurious currents. Attempts are being made at this time to implement alternative numerics that are capable of capturing steeper gradients. In this manner, the low density regions can be further reduced, which will lead to a greater reduction of the spurious currents. These improvements can lead to more accurate and more stable simulation results using the lattice Boltzmann method.

- [1] G. Ryskin, L. G. Leal, Numerical solution of free-boundary problems in fluid mechanics. Part 2. Buoyancy-driven motion of a gas bubble through a quiescent liquid, *Journal of Fluid Mechanics* 148 (1984) 19–35.
- [2] G. Tryggvason, B. Bunner, A. Esmaeeli, D. Juric, N. Al-Rawahi, W. Tauber, J. Han, S. Nas, Y.-J. Jan, A front-tracking method for the computations of multiphase flow, *Journal of Computational Physics* 169 (2) (2001) 708 – 759. doi:10.1006/jcph.2001.6726.
- [3] S. S. Yoon, S. D. Heister, A nonlinear atomization model based on a boundary layer instability mechanism, *Physics of Fluids* 16 (1) (2004) 47–61. doi:10.1063/1.1629301.
- [4] F. H. Harlow, J. E. Welch, Numerical calculation of time-dependent viscous incompressible flow of fluid with free surface, *Physics of Fluids* 8 (12) (1965) 2182–2189. doi:10.1063/1.1761178.
- [5] B. J. Daly, Numerical study of the effect of surface tension on interface instability, *Physics of Fluids* 12 (7) (1969) 1340–1354. doi:10.1063/1.1692673.
- [6] C. Hirt, B. Nichols, Volume of fluid (VOF) method for the dynamics of free boundaries, *Journal of Computational Physics* 39 (1) (1981) 201 – 225. doi:10.1016/0021-9991(81)90145-5.
- [7] J. Sethian, *Level Set Methods and Fast Marching Methods: Evolving Interfaces in Computational Geometry, Fluid Mechanics, Computer Vision, and Materials Science*, Cambridge Monographs on Applied and Computational Mathematics, Cambridge University Press, 1999.
- [8] M. R. Swift, W. R. Osborn, J. M. Yeomans, Lattice Boltzmann simulation of nonideal fluids, *Phys. Rev. Lett.* 75 (1995) 830–833. doi:10.1103/PhysRevLett.75.830.
- [9] M. R. Swift, E. Orlandini, W. R. Osborn, J. M. Yeomans, Lattice Boltzmann simulations of liquid-gas and binary fluid systems, *Phys. Rev. E* 54 (1996) 5041–5052. doi:10.1103/PhysRevE.54.5041.
- [10] X. Shan, H. Chen, Lattice Boltzmann model for simulating flows with multiple phases and components, *Phys. Rev. E* 47 (3) (1993) 1815–1819.
- [11] X. Shan, H. Chen, Simulation of nonideal gases and liquid-gas phase transitions by the lattice Boltzmann equation, *Phys. Rev. E* 49 (4) (1994) 2941–2948.
- [12] X. Shan, G. Doolen, Multicomponent lattice-Boltzmann model with interparticle interaction, *Journal of Statistical Physics* 81 (1995) 379–393.
- [13] P. Yuan, Thermal lattice Boltzmann two-phase flow model for fluid dynamics, Ph.D. thesis, University of Pittsburgh (2005).
- [14] P. Yuan, L. Schaefer, Equations of state in a lattice Boltzmann model, *Physics of Fluids* 18 (4) (2006) 042101.
- [15] A. L. Kupershtokh, C. Stamatelatos, D. P. Agoris, Stochastic model of partial discharge activity in liquid and solid dielectrics, in: *Proc. of the 15th IEEE Conf.*

- on Dielectric Liquids, Coimbra, Portugal, 2005, pp. 135–138.
- [16] A. L. Kupershtokh, Simulation of flows with liquid-vapor interfaces by the lattice Boltzmann method, *Vestnik NGU (Quart. J. of Novosibirsk State Univ.)*, Series: Math., Mech. and Informatics (in Russian) 5 (3) (2005) 29–42.
- [17] R. Nourgaliev, T. Dinh, T. Theofanous, D. Joseph, The lattice Boltzmann equation method: theoretical interpretation, numerics and implications, *International Journal of Multiphase Flow* 29 (1) (2003) 117 – 169. doi:10.1016/S0301-9322(02)00108-8.
- [18] J. Bao, L. Schaefer, Lattice Boltzmann equation model for multi-component multi-phase flow with high density ratios, *Applied Mathematical Modelling* 37 (4) (2013) 1860–1871. doi:10.1016/j.apm.2012.04.048.
- [19] P. L. Bhatnagar, E. P. Gross, M. Krook, A model for collision processes in gases. I. Small amplitude processes in charged and neutral one-component systems, *Phys. Rev.* 94 (1954) 511–525. doi:10.1103/PhysRev.94.511.
- [20] Y. H. Qian, D. D’Humières, P. Lallemand, Lattice BGK models for Navier-Stokes equation, *EPL (Europhysics Letters)* 17 (6) (1992) 479.
- [21] H. Chen, S. Chen, W. H. Matthaeus, Recovery of the Navier-Stokes equations using a lattice-gas Boltzmann method, *Phys. Rev. A* 45 (1992) R5339–R5342. doi:10.1103/PhysRevA.45.R5339.
- [22] X. Shan, X.-F. Yuan, H. Chen, Kinetic theory representation of hydrodynamics: a way beyond the Navier-Stokes equation, *Journal of Fluid Mechanics* 550 (1) (2006) 413–441. doi:10.1017/S0022112005008153.
- [23] X. Shan, X. He, Discretization of the velocity space in the solution of the Boltzmann equation, *Phys. Rev. Lett.* 80 (1998) 65–68. doi:10.1103/PhysRevLett.80.65.
- [24] X. He, G. D. Doolen, Thermodynamic foundations of kinetic theory and lattice Boltzmann models for multiphase flows, *Journal of Statistical Physics* 107 (4) (2002) 309–328.
- [25] X. He, L.-S. Luo, Theory of the lattice Boltzmann method: From the Boltzmann equation to the lattice Boltzmann equation, *Phys. Rev. E* 56 (1997) 6811–6817. doi:10.1103/PhysRevE.56.6811.
- [26] S. Chen, G. D. Doolen, Lattice Boltzmann method for fluid flows, *Annual Review of Fluid Mechanics* 30 (1) (1998) 329–364. doi:10.1146/annurev.fluid.30.1.329.
- [27] A. L. Kupershtokh, New method of incorporating a body force term into the lattice Boltzmann equation, in: *5th International EHD Workshop, Poitiers, France, 2004*, pp. 241–246.
- [28] J. Bao, High density ratio multi-component lattice Boltzmann flow model for fluid dynamics and CUDA parallel computation, Ph.D. thesis, University of Pittsburgh (2010).
- [29] I. Ginzbourg, P. M. Adler, Boundary flow condition analysis for the three-dimensional lattice Boltzmann model, *J. Phys. II France* 4 (2) (1994) 191–214. doi:10.1051/jp2:1994123.
- [30] S. Succi, *The lattice Boltzmann equation for fluid dynamics and beyond*, Numerical mathematics and scientific computation, Clarendon Press, 2001.
- [31] M. Sukop, D. Thorne, *Lattice Boltzmann modeling: an introduction for geoscientists and engineers*, Springer, 2006.
- [32] A. Kupershtokh, D. Medvedev, D. Karpov, On equations of state in a lattice Boltzmann method, *Computers & Mathematics with Applications* 58 (5) (2009) 965 – 974.
- [33] Q. Kang, D. Zhang, S. Chen, Displacement of a two-dimensional immiscible droplet in a channel, *Physics of Fluids* 14 (9) (2002) 3203–3214.
- [34] C. Hirsch, *Numerical computation of internal and external flows: fundamentals of computational fluid dy-*

- namics, 2nd Edition, Butterworth-Heinemann, 2007.
- [35] X. Shan, Simulation of Rayleigh-Bénard convection using a lattice Boltzmann method, *Phys. Rev. E* 55 (1997) 2780–2788. doi:10.1103/PhysRevE.55.2780.
- [36] K. Kono, T. Ishizuka, H. Tsuda, A. Kurosawa, Application of lattice Boltzmann model to multiphase flows with phase transition, *Computer Physics Communications* 129 (1-3) (2000) 110 – 120. doi:10.1016/S0010-4655(00)00098-9.
- [37] R. Zhang, H. Chen, Lattice Boltzmann method for simulations of liquid-vapor thermal flows, *Phys. Rev. E* 67 (2003) 066711. doi:10.1103/PhysRevE.67.066711.
- [38] S. Gong, P. Cheng, A lattice Boltzmann method for simulation of liquid–vapor phase-change heat transfer, *International Journal of Heat and Mass Transfer* 55 (17–18) (2012) 4923 – 4927.
- [39] S. Gong, P. Cheng, Numerical investigation of droplet motion and coalescence by an improved lattice Boltzmann model for phase transitions and multiphase flows, *Computers & Fluids* 53 (0) (2012) 93 – 104.
- [40] S. Gong, P. Cheng, Lattice Boltzmann simulation of periodic bubble nucleation, growth and departure from a heated surface in pool boiling, *International Journal of Heat and Mass Transfer* 64 (0) (2013) 122–132.
- [41] Q. Zou, X. He, On pressure and velocity boundary conditions for the lattice Boltzmann BGK model, *Physics of Fluids* 9 (6) (1997) 1591–1598.
- [42] J. Latt, B. Chopard, Straight velocity boundaries in the lattice Boltzmann method, *Physical Review E* 77 (5) (2008) 1–16.
- [43] Z. Yu, A novel lattice Boltzmann method for direct numerical simulation of multiphase flows, Ph.D. thesis, Ohio State University (2009).
- [44] E. W. Lemmon, M. O. McLinden, D. G. Friend, Thermophysical properties of fluid systems, in: P. Linstrom, W. Mallard (Eds.), NIST Chemistry Web-Book, NIST Standard Reference Database Number 69, National Institute of Standards and Technology, Gaithersburg, MD, 2013.

List of Figures

1	The D2Q9 lattice structure utilizing nine velocities in two dimensions (including the zeroth velocity).	24
2	The pseudopotential that results from the formulation of the effective mass using the Peng-Robinson equation of state for the pressure calculation. The attractive core and repulsive tail mimic that of molecular interactions.	25
3	Comparison of different methods of approximating the gradient operator in the interparticle interaction force equation. The linear combination gradient approximation (LCGA) developed by Kupershtokh is shown to perform the best [15, 16, 32].	26
4	The numerical grids for each chemical component showing reduced density contours of a typical 2D, two phase, two component droplet simulation.	27
5	Reduced density cross-sections of a liquid water droplet in air.	28
6	Reduced density cross-sections of a liquid water droplet in air showing invalid, miscible results at $T = 550$ K.	29
8	Overlap of the stable regions of the intercomponent interaction parameters from 450 K to 625 K.	31
9	Grid independence verification of the 2D, two component, thermal conduction simulation.	32
10	Initial reduced density contours showing the two liquid layers (red) and zero-density regions (blue) on the two grids and the initial temperature cross-section of the 2D, two component, thermal conduction simulation.	33
11	Reduced temperature cross-sections of grid one showing the time evolution of the thermal profile of the 2D, two component, thermal conduction simulation. Each line represents a single timestep, with darker colors corresponding to increasing times.	34
12	Final reduced density cross-sections and reduced temperature contours of grid one of the 2D, two component, thermal conduction simulation.	35
13	Residual temperature error between the simulation results and the theoretical solution as the 2D, two component thermal conduction simulation evolves through time.	36
14	Temperature and velocity errors that result from using different coupling models in the MPiMC-T model as the thermal conduction simulation evolves through time.	37
15	Comparison of the evolution of the total temperature in the domain using different coupling models in the MPiMC-T LB model for a static droplet simulation.	38
16	Temperature and velocity errors that result from relaxing the coupling requirements in the MPiMC-T model as the static droplet simulation evolves through time. Note that the results from TC, VC, and TCVC all overlap for the temperature errors, but only the results from VC and TCVC overlap for the velocity errors.	39
17	Comparison of the spurious currents in the steady-state static droplet simulation at 500 K, using the model with no coupling and the model with both temperature and velocity-coupling. Note that while the velocities are plotted over the entire domain in both figures, the weighting by the low density regions reduces the magnitudes significantly in the second figure.	40

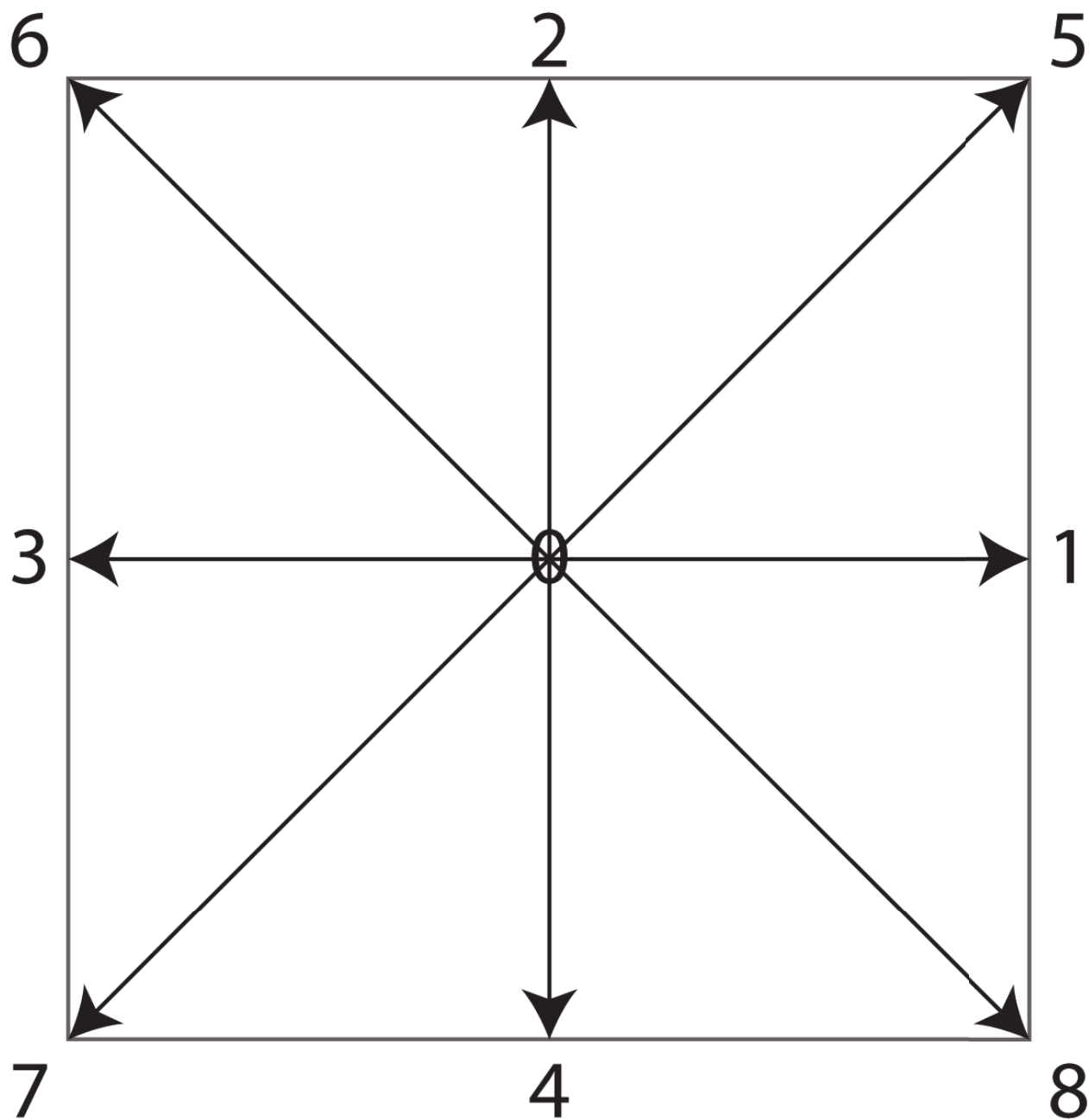


Figure 1: The D2Q9 lattice structure utilizing nine velocities in two dimensions (including the zeroth velocity).

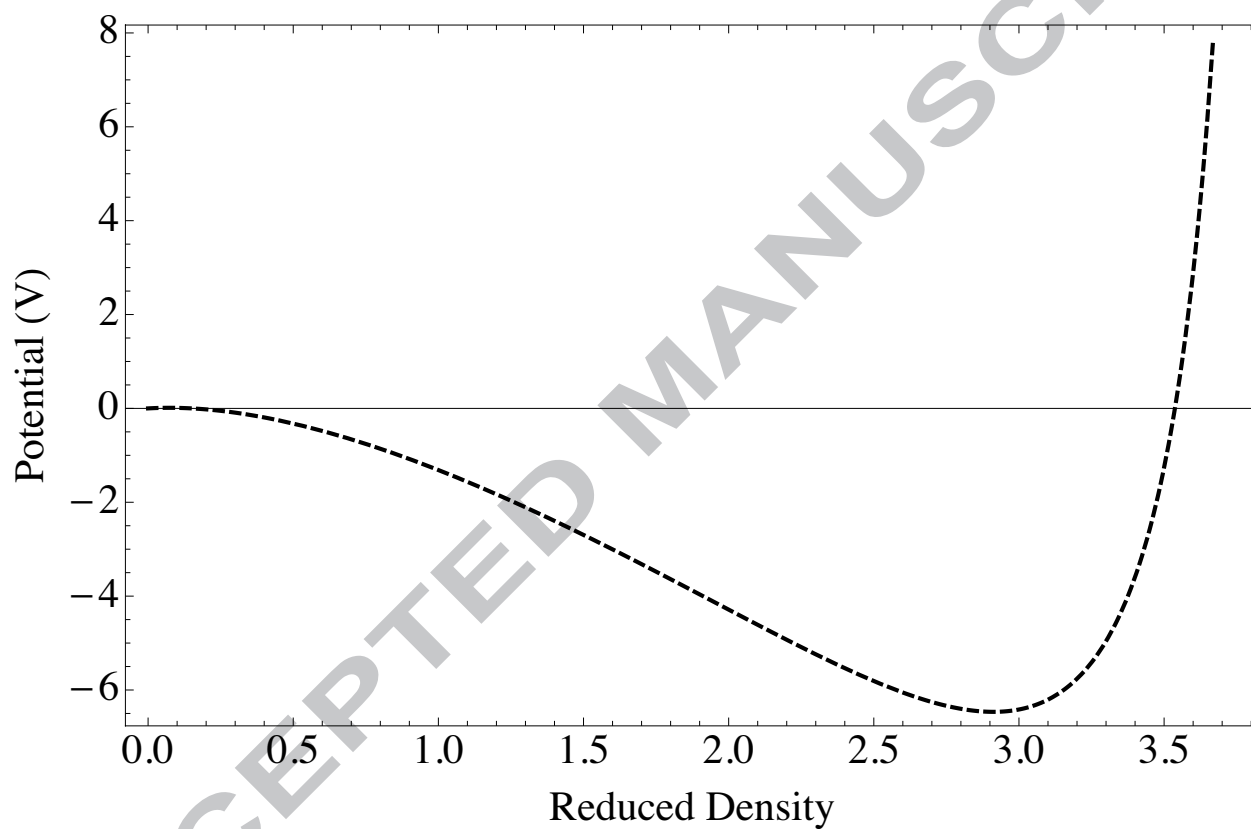


Figure 2: The pseudopotential that results from the formulation of the effective mass using the Peng-Robinson equation of state for the pressure calculation. The attractive core and repulsive tail mimic that of molecular interactions.

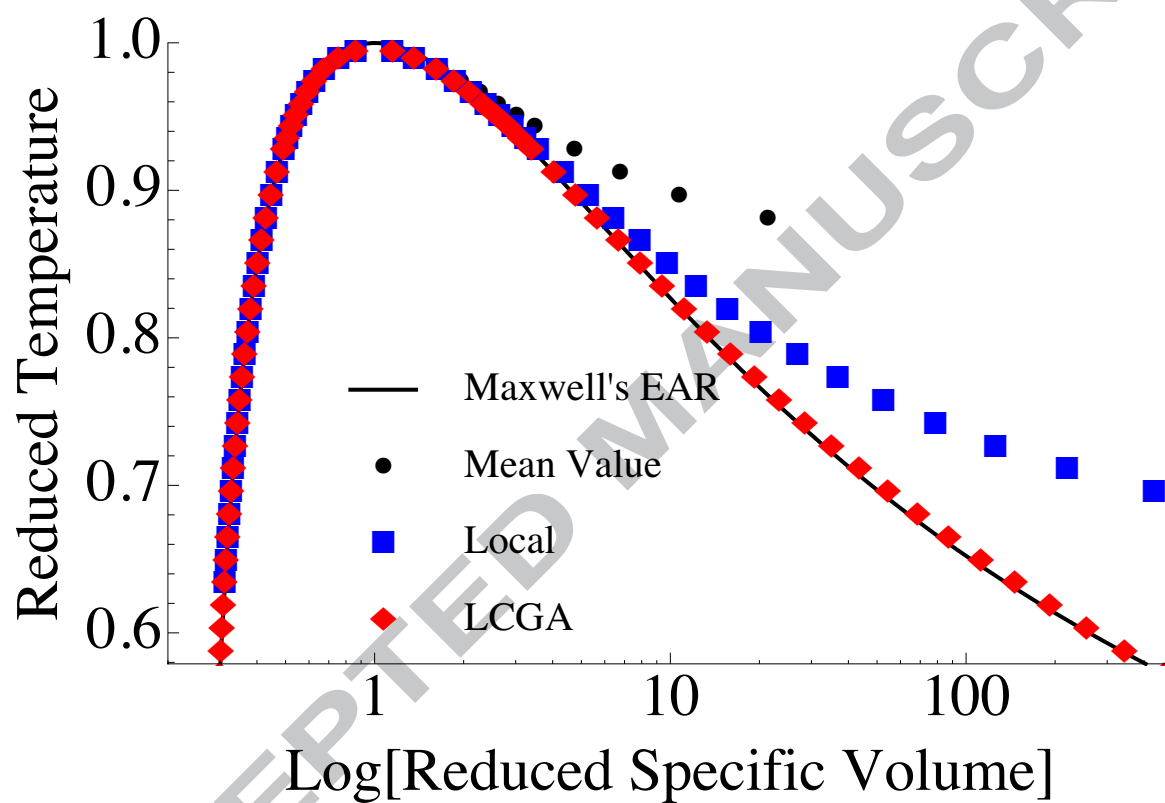
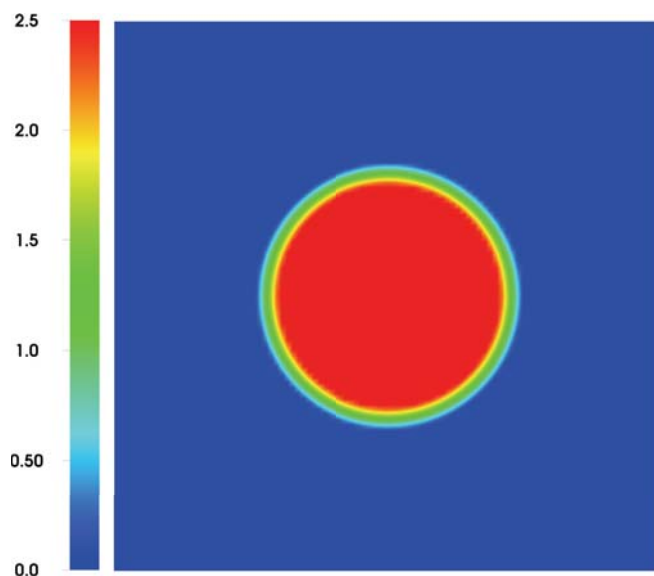
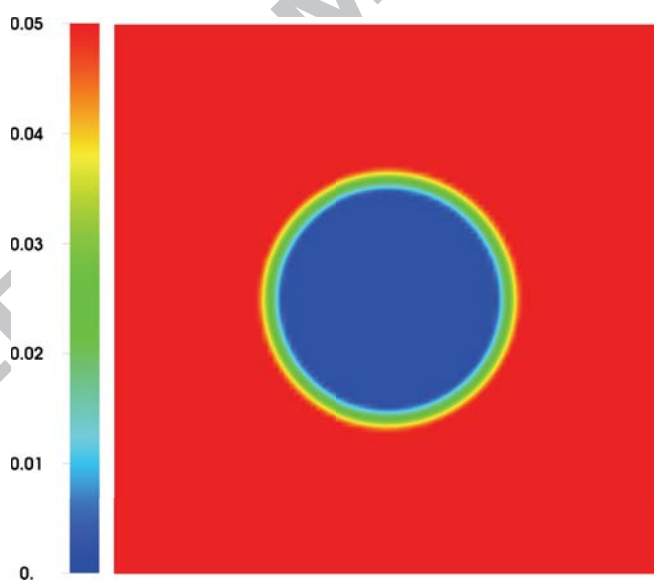


Figure 3: Comparison of different methods of approximating the gradient operator in the interparticle interaction force equation. The linear combination gradient approximation (LCGA) developed by Kupershtokh is shown to perform the best [15, 16, 32].

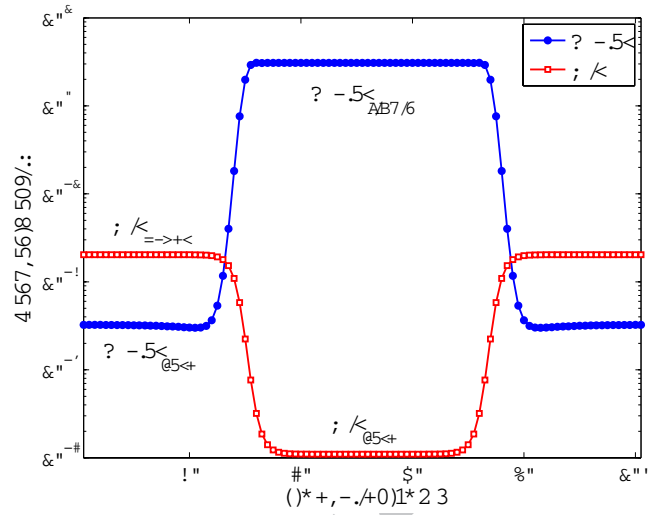


(a) Grid one: Liquid droplet of Component *A* (red) surrounded by a zero-density region (blue).

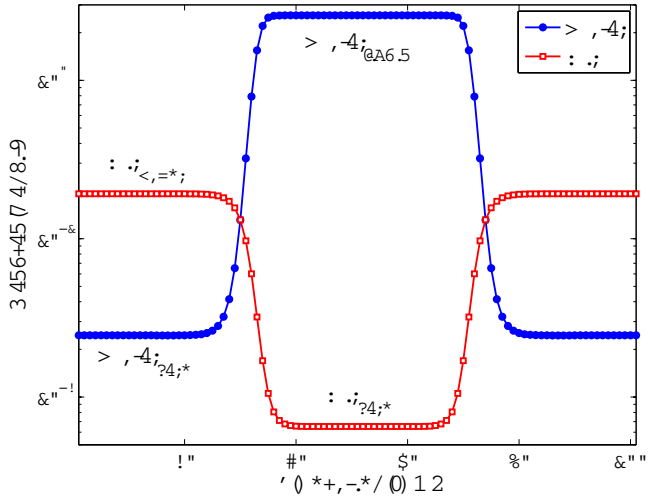


(b) Grid two: Vapor region of Component *B* (red) surrounding a zero-density region (blue).

Figure 4: The numerical grids for each chemical component showing reduced density contours of a typical 2D, two phase, two component droplet simulation.



(a) Valid, immiscible results at $T = 450$ K. Reduced densities: $\rho_{liq} = 3.07$, $\rho_{vap} = 0.02$



(b) Valid, immiscible results at $T = 600$ K. Reduced densities: $\rho_{liq} = 2.57$, $\rho_{vap} = 0.19$

Figure 5: Reduced density cross-sections of a liquid water droplet in air.

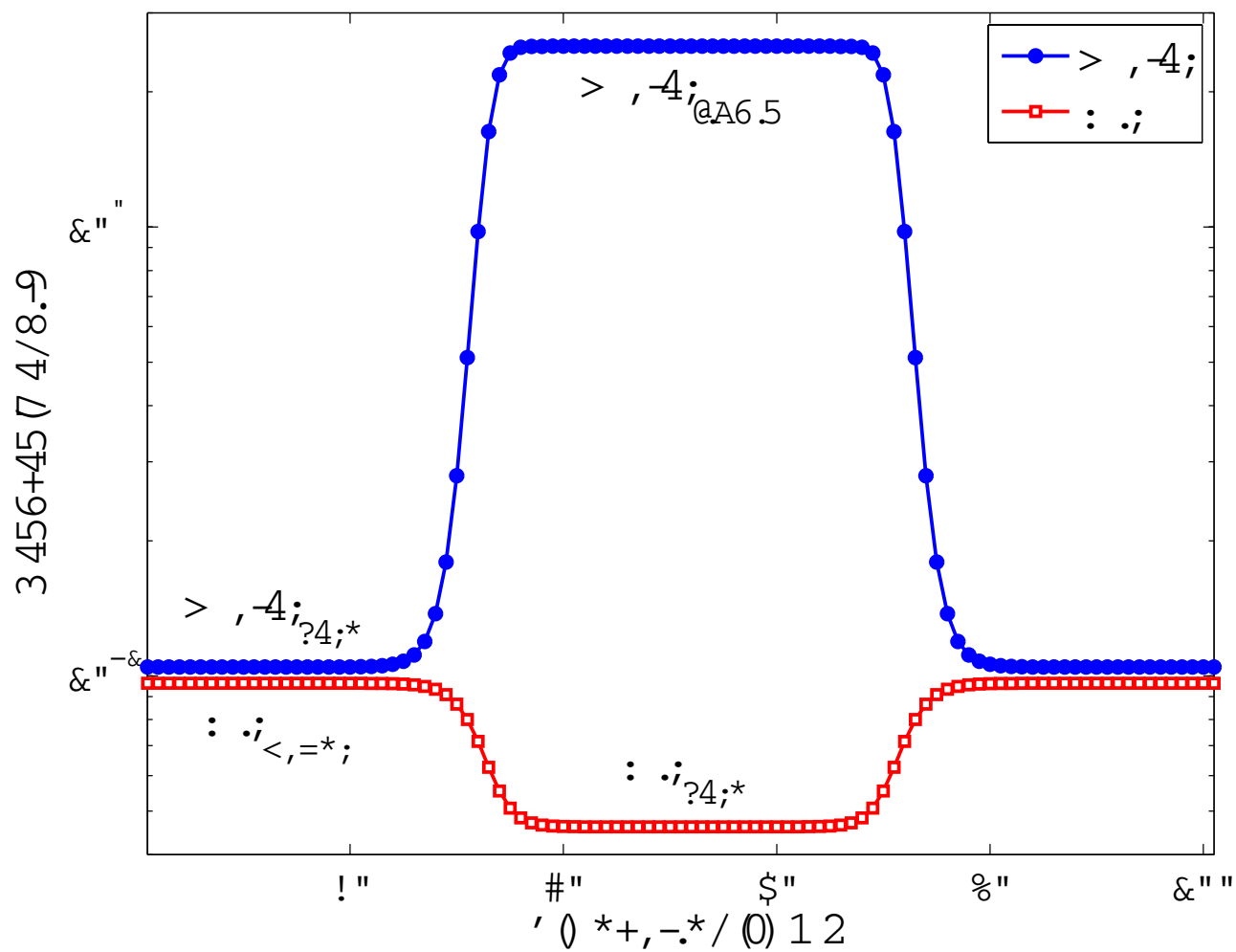
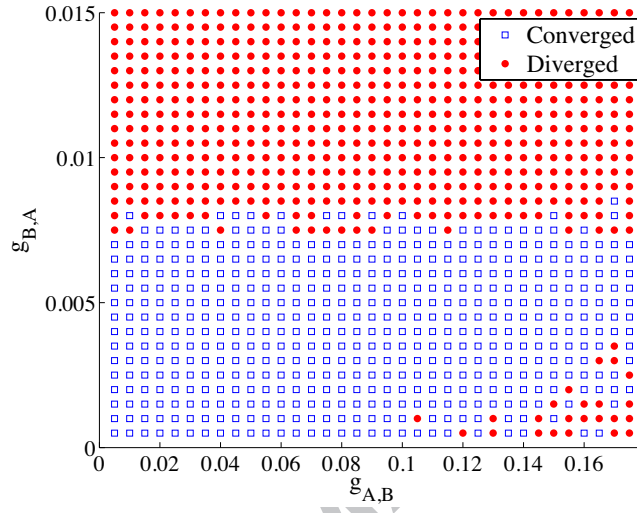
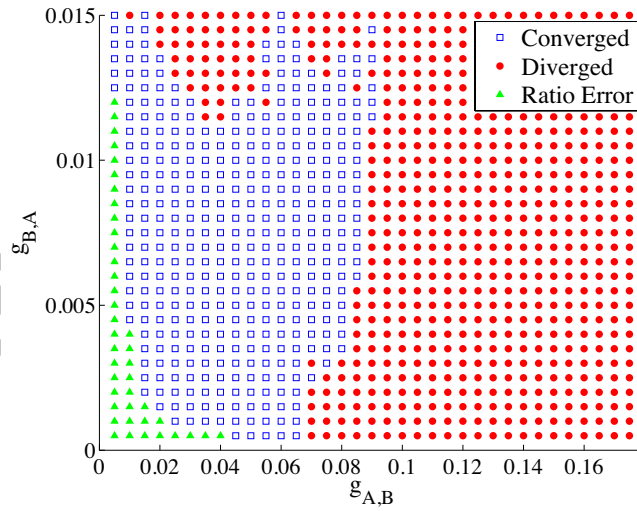


Figure 6: Reduced density cross-sections of a liquid water droplet in air showing invalid, miscible results at $T = 550$ K.



(a) $T = 450$ K



(b) $T = 625$ K

Figure 7: Stability region analysis of intercomponent interaction parameters at the specified temperatures.

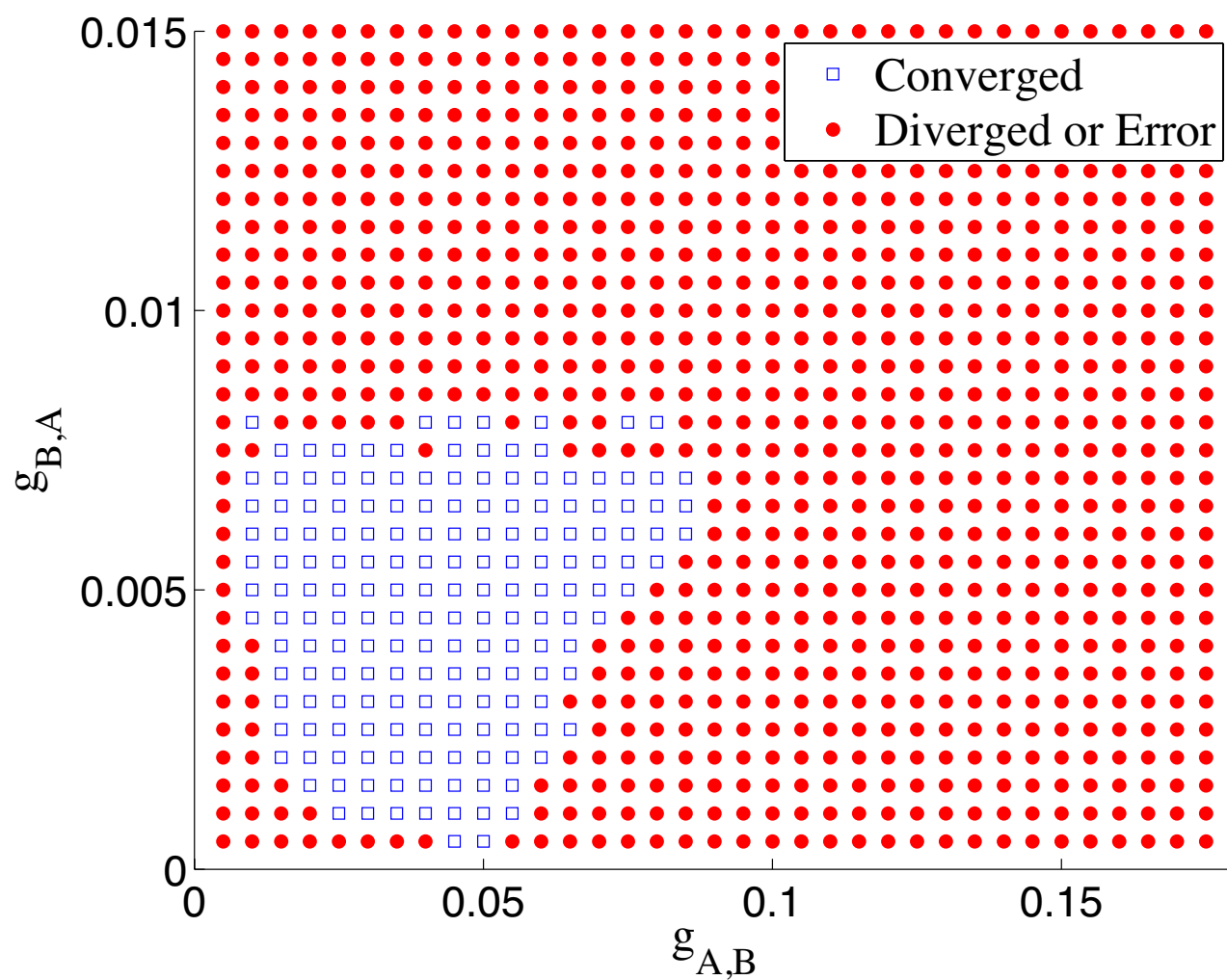


Figure 8: Overlap of the stable regions of the intercomponent interaction parameters from 450 K to 625 K.

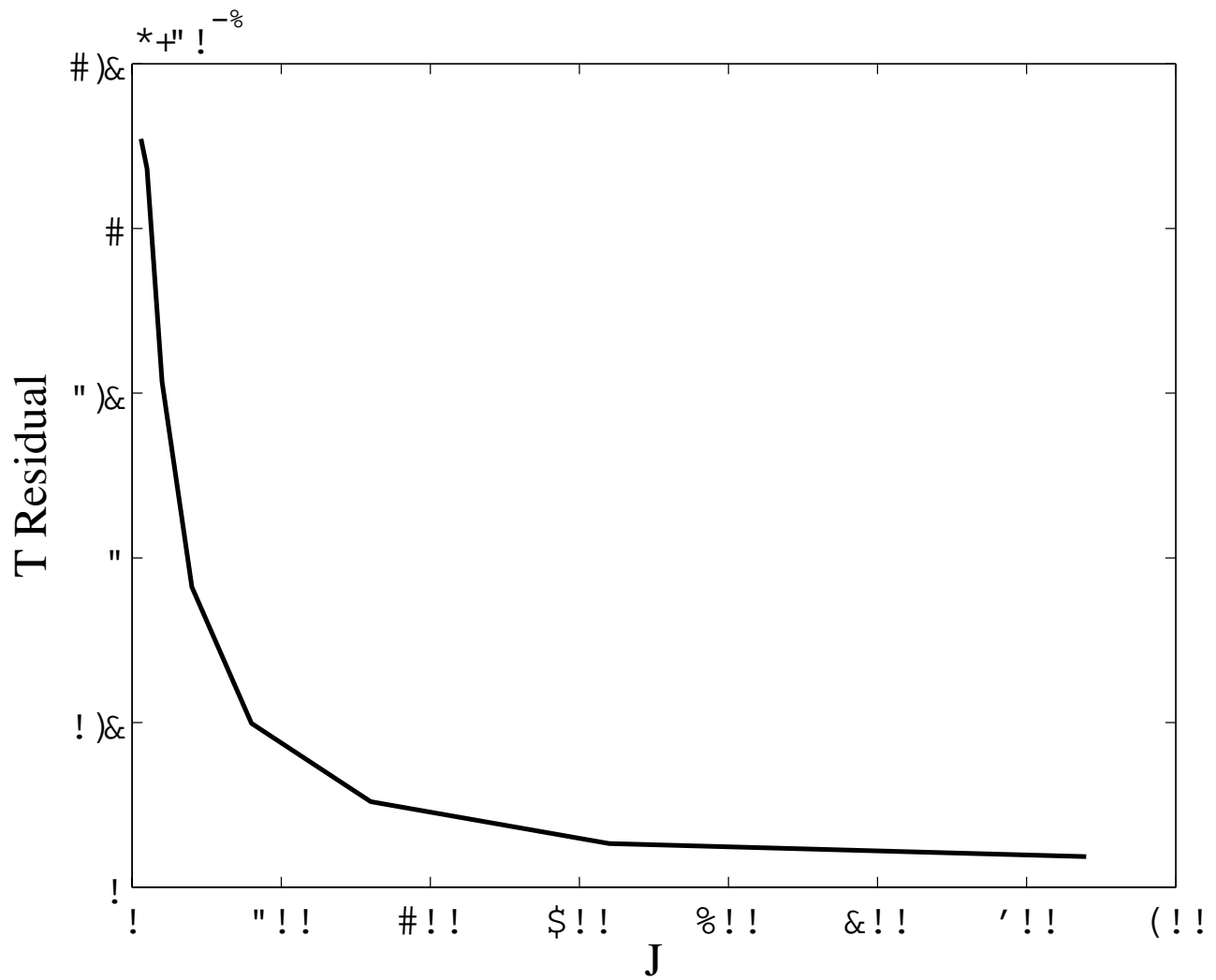


Figure 9: Grid independence verification of the 2D, two component, thermal conduction simulation.

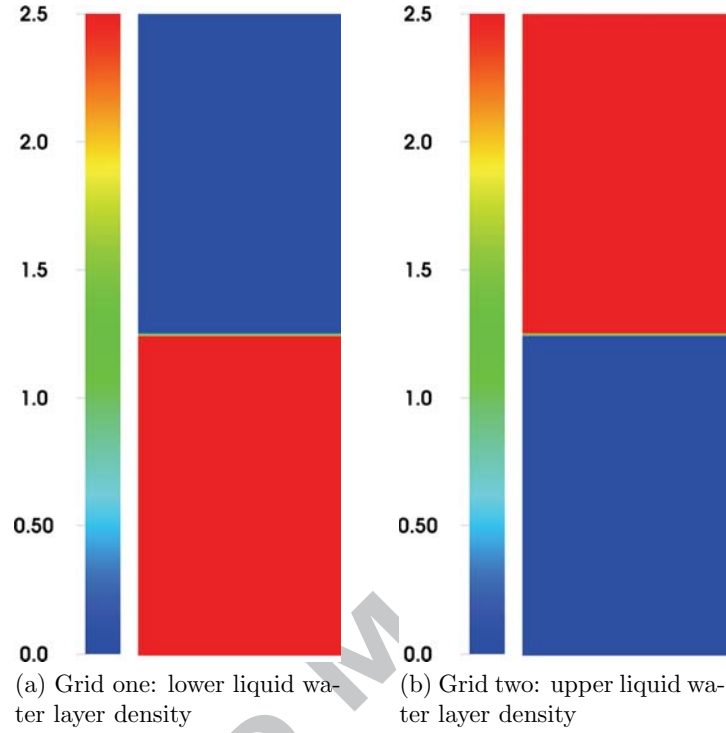


Figure 10: Initial reduced density contours showing the two liquid layers (red) and zero-density regions (blue) on the two grids and the initial temperature cross-section of the 2D, two component, thermal conduction simulation.

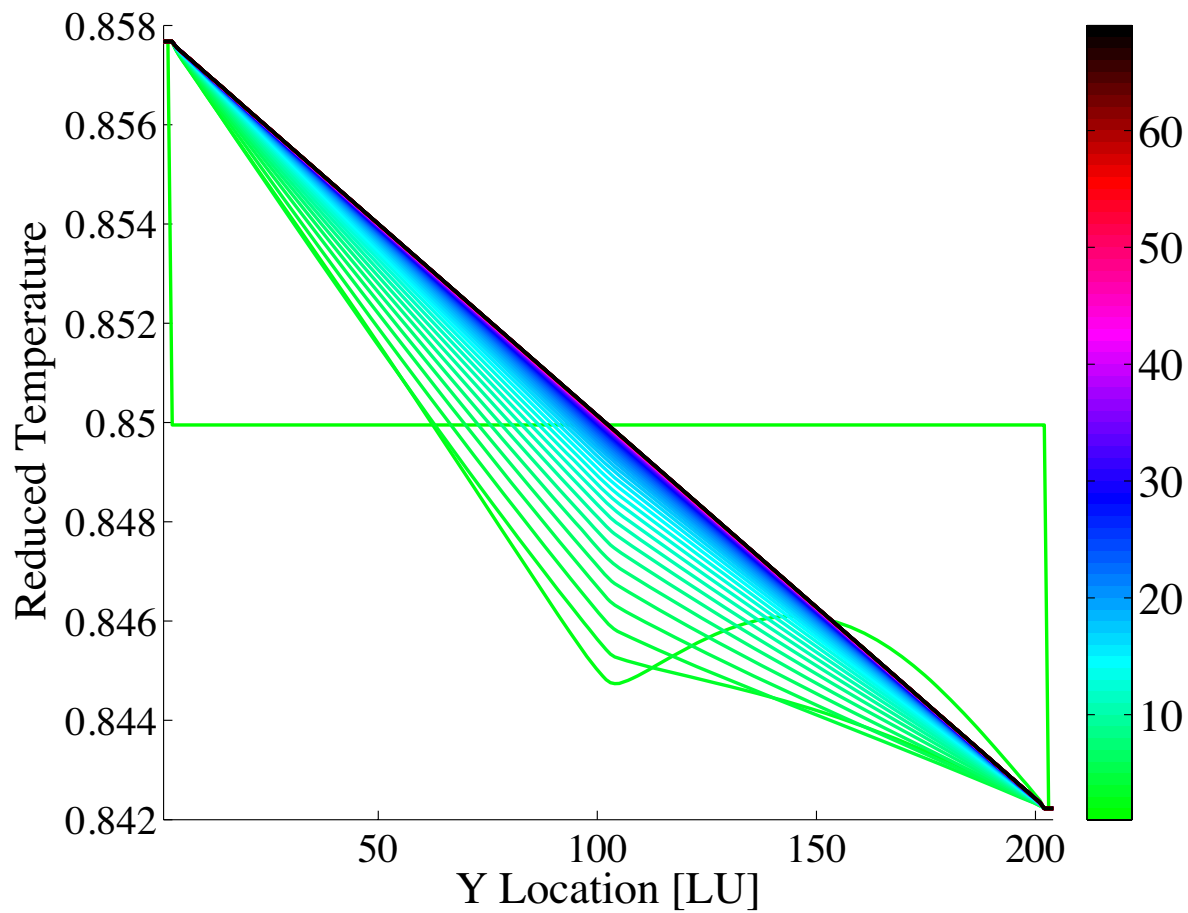
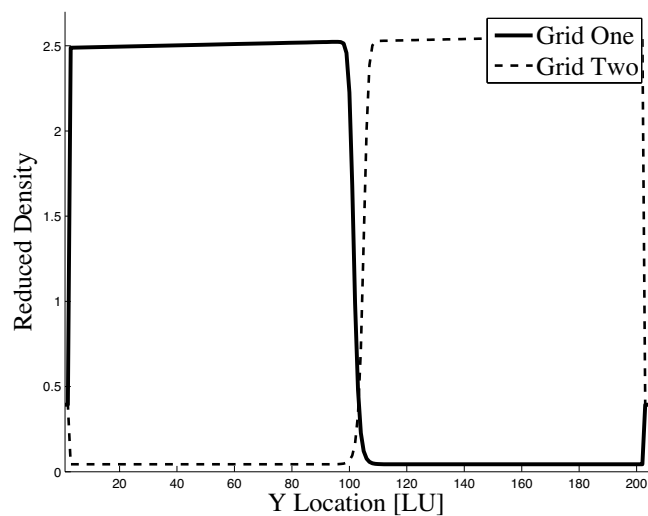
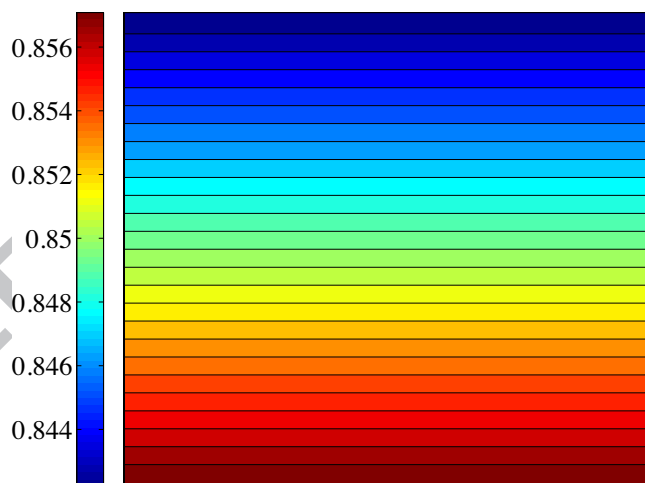


Figure 11: Reduced temperature cross-sections of grid one showing the time evolution of the thermal profile of the 2D, two component, thermal conduction simulation. Each line represents a single timestep, with darker colors corresponding to increasing times.



(a) Final density cross-section



(b) Final temperature contours

Figure 12: Final reduced density cross-sections and reduced temperature contours of grid one of the 2D, two component, thermal conduction simulation.

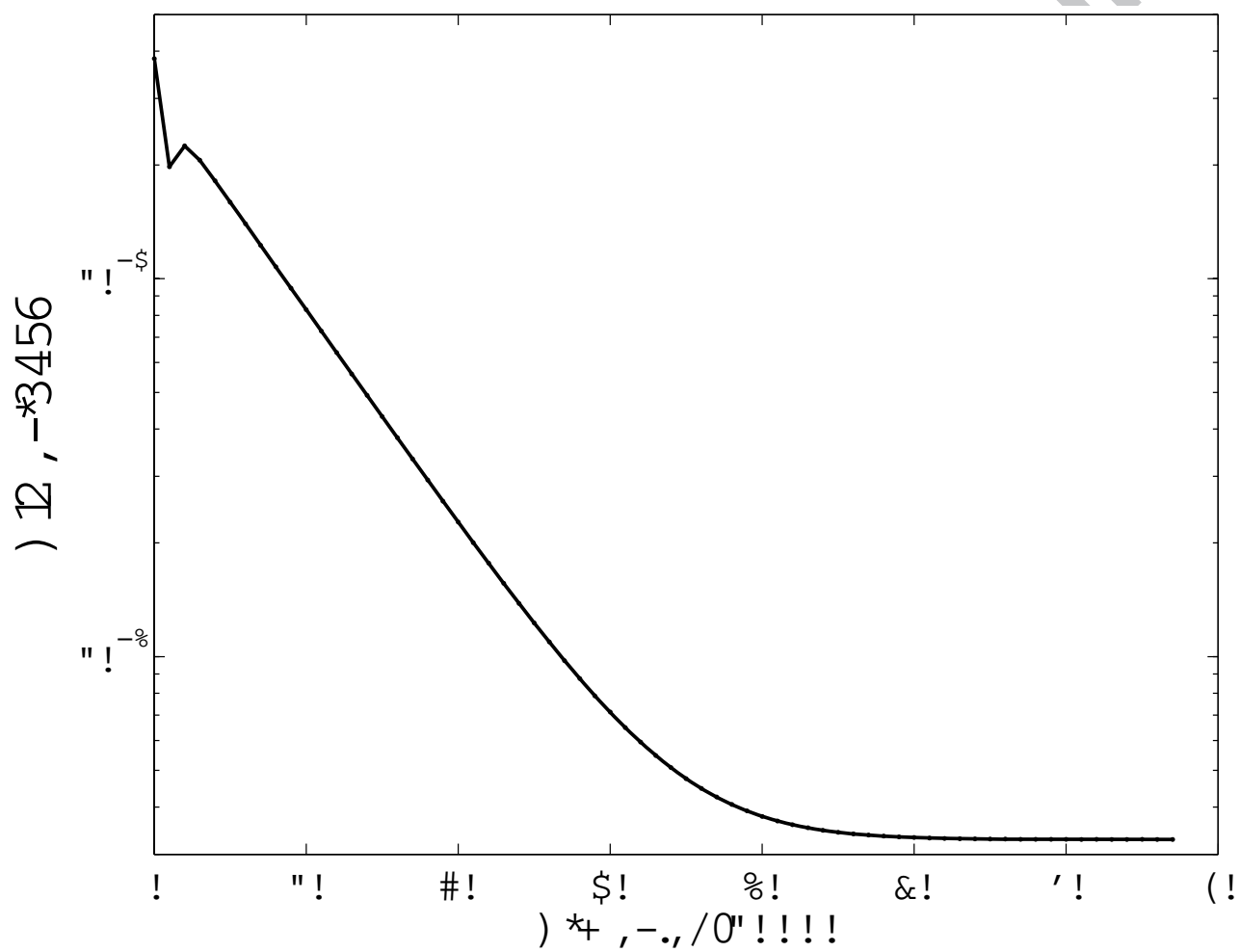
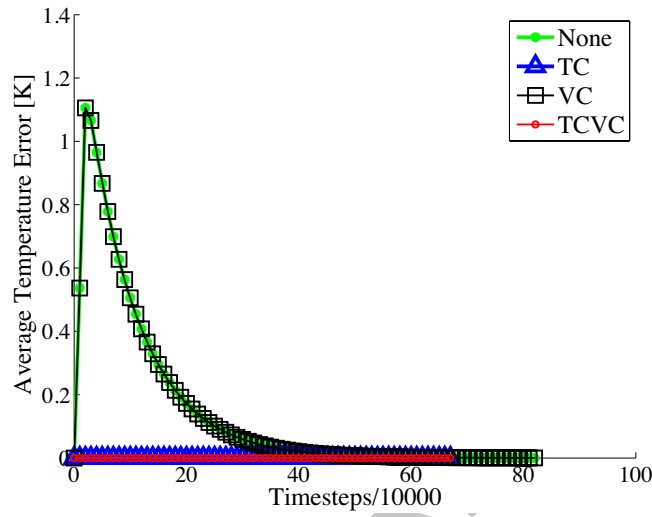
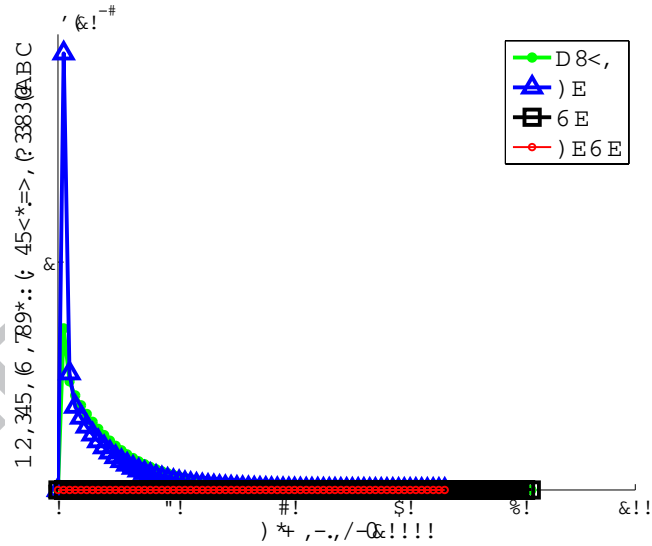


Figure 13: Residual temperature error between the simulation results and the theoretical solution as the 2D, two component thermal conduction simulation evolves through time.



(a) Temperature errors



(b) Velocity magnitude errors

Figure 14: Temperature and velocity errors that result from using no coupling of the macroscopic variables (None), only the temperature-coupling model (TC), only the velocity-coupling model (VC), and the temperature and velocity-coupling models used together (TCVC) in the MPiMC-T model as the thermal conduction simulation evolves through time. Note that for the temperature errors, TC and TCVC overlap and None and VC overlap, and for the velocity errors, VC and TCVC overlap.

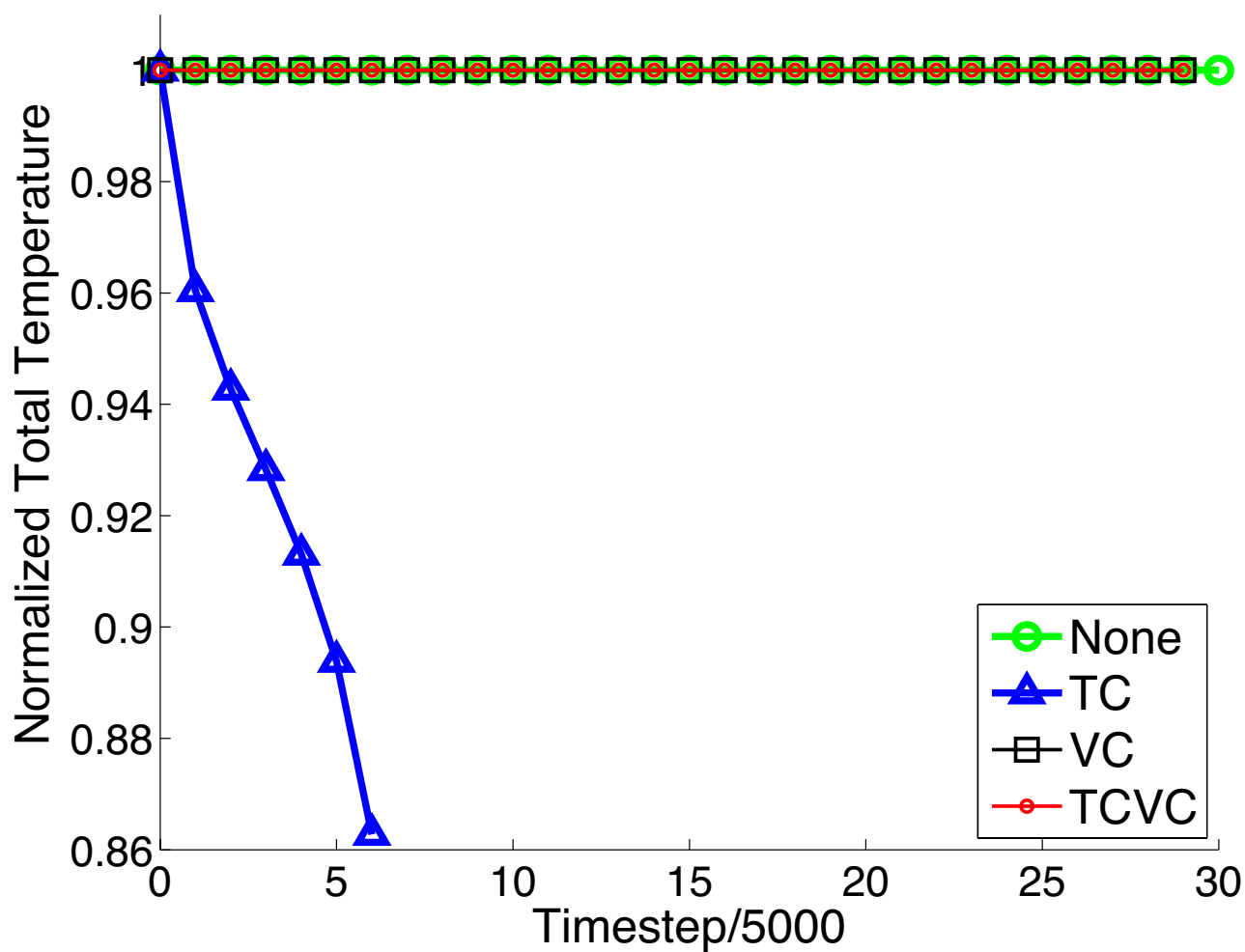
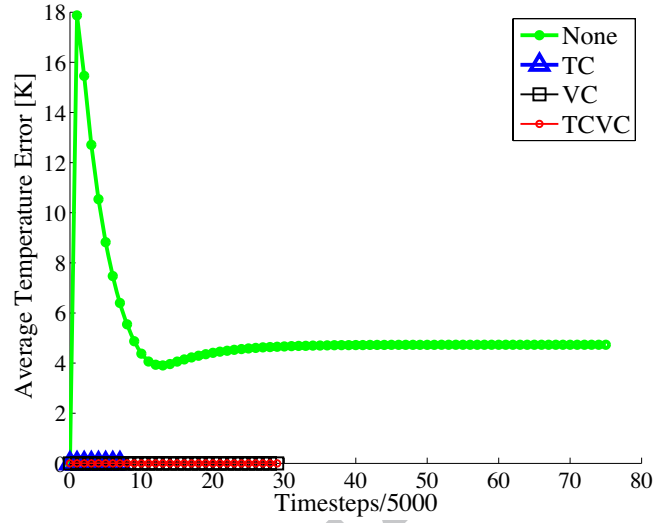
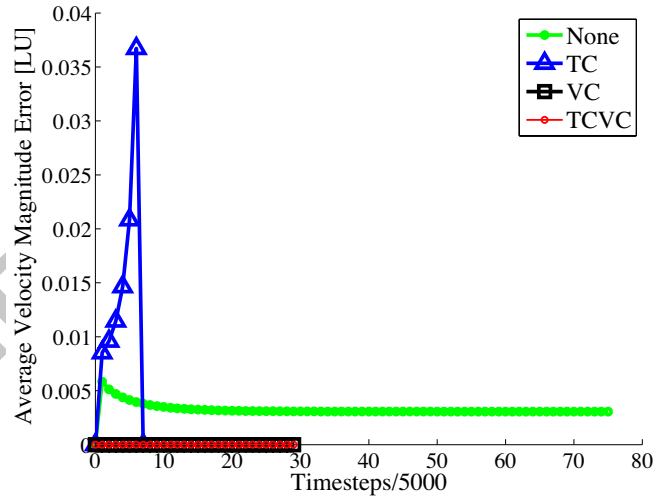


Figure 15: Comparison of the evolution of the total temperature in the domain using no coupling of the macroscopic variables (None), only the temperature-coupling model (TC), only the velocity-coupling model (VC), and the temperature and velocity-coupling models used together (TCVC) in the MPiMC-T LB model for a static droplet simulation. Note that the results from None, VC, and TCVC all overlap.

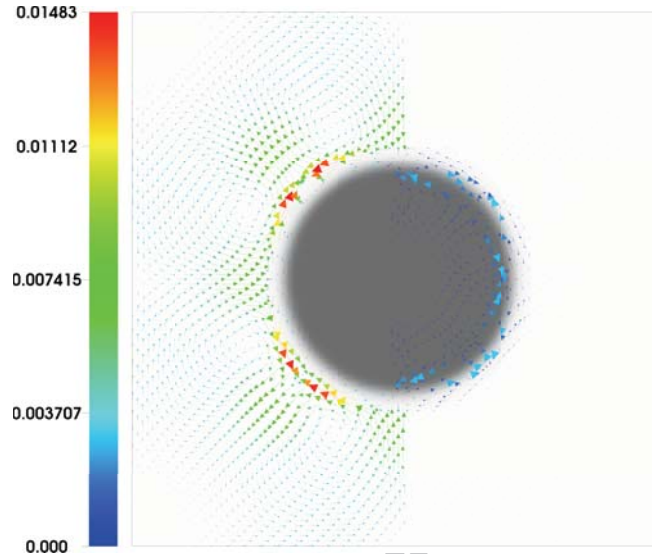


(a) Temperature errors

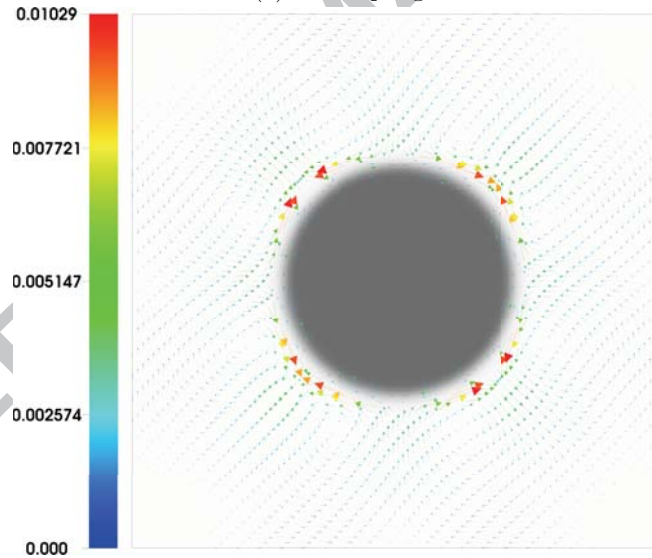


(b) Velocity magnitude errors

Figure 16: Temperature and velocity errors that result from relaxing the coupling requirements in the MPiMC-T model as the static droplet simulation evolves through time. Note that the results from TC, VC, and TCVC all overlap for the temperature errors, but only the results from VC and TCVC overlap for the velocity errors.



(a) No coupling



(b) TCVC Coupling

Figure 17: Comparison of the spurious currents in the steady-state static droplet simulation at 500 K, using the model with no coupling and the model with both temperature and velocity-coupling. Note that while the velocities are plotted over the entire domain in both figures, the weighting by the low density regions reduces the magnitudes significantly in the second figure.

- Stability region analysis of multiphase LB interparticle interaction parameters
- Construction of a multiphase, immiscible, multicomponent, thermal LB model
- Validation using static thermal conduction and steady-state droplet simulations
- Conservation properties and physical consistency maintained in immiscible limit
- A reduction of spurious currents is achieved for immiscible simulations

ACCEPTED MANUSCRIPT